Bulletin of Volcanology (2025) 87:18
https://doi.org/10.1007/s00445-025-01802-7

RESEARCH ARTICLE

The 1956 eruption of Bezymianny volcano (Kamchatka)—part I: petrological constraints on magma storage and eruptive dynamics

Caroline Martel[1] · Saskia Erdmann[1] · Georges Boudon[2] · Hélène Balcone-Boissard[3] · Léa Ostorero[2,4] · Thiebaut d'Augustin[3] · Alexander Belousov[5] · Marina Belousova[5] · Vesta O. Davydova[6] · Vasily D. Shcherbakov[6]

Received: 5 April 2024 / Accepted: 31 January 2025

Abstract

Bezymianny volcano (Kamchatka, Russia) is an andesitic island arc stratovolcano that started to erupt in 1955 after ~ 1000 years of dormancy. On March 30, 1956, the climactic phase of the eruption was preceded by a 4-month-long emplacement of a shallow cryptodome, which triggered a flank collapse violently decompressing the magma into a laterally directed blast followed by an explosive phase emplacing extensive pumice concentrated pyroclastic density currents (pumice C-PDC). Aiming at constraining the plumbing system below Bezymianny volcano prior to the 1956 eruption, we performed a multiphase textural and petrological study using dense to vesiculated clasts of the blast and pumice samples from the post-blast C-PDC deposits. We inferred the pressure and temperature conditions of magma storage using sample vesicularity, amphibole destabilization rims, volatile contents in melt inclusions, microlite textures, and phase compositions (phenocrysts, microlites, and glasses). We propose a three-level magma storage characterized by a deep reservoir ($\geq$ 200–350 MPa, $\geq$ 840 °C, ~ 4.0–8.0 wt% H_2O and CO_2 up to 1500 ppm, where amphibole is stable), a shallow reservoir (50–100 MPa, 850–900 °C, 1.5–4.0 wt% H_2O and CO_2 < 250 ppm, where amphibole is unstable and quartz crystallizes) in which the pre-cryptodome magma resided and from which the post-blast pumiceous magma originated, and a subsurface cryptodome (< 25 MPa, ~ 900 °C, cristobalite crystallized) from which the blast was initiated. This plumbing system provides the framework for constraining the timescales of the 1956 eruptive dynamics (companion paper). The three-stage architecture proposed for the 1956 andesitic reservoir compares to the present-day plumbing system emitting mafic lavas, thus suggesting that the timescales of the eruptive dynamics (e.g., magma residence time and ascent rate) may be the key to determining evolved or mafic magmas.

Keywords Magma storage · Amphibole · Decomposition rims · Melt inclusion composition · Microlite · Silica polymorphs · Thermobarometry

Editorial responsibility: J. Gardner

✉ Caroline Martel
caroline.martel@cnrs-orleans.fr

[1] Institut des Sciences de La Terre d'Orléans (ISTO), UMR 7327, Univ Orléans, CNRS, BRGM, OSUC, Orléans, France

[2] Institut de physique du globe de Paris (IPGP), Université Paris Cité, CNRS, 75005 Paris, France

[3] Institut Des Sciences de La Terre de Paris (ISTeP), UMR 7193, CNRS-Sorbonne Université, Paris, France

[4] Department of Earth and Environmental Sciences, University of Milan-Bicocca, Milan, Italy

[5] Institute of Volcanology and Seismology, 9 Piip Boulevard, Petropavlovsk-Kamchatsky 683006, Russia

[6] Geological Departments, Lomonosov Moscow State University, Leninskii Gory, 1, 119191 Moscow, Russia

Introduction

Island arc volcanism involving differentiated magmas (andesites to rhyolites) is one of the most dreaded types due to the violence of the eruptions and our difficulty to predict the eruption time, style, and damage extent. Andesitic stratovolcanoes commonly produce effusive growth of lava domes, whose collapse generates low-energy concentrated pyroclastic density currents (C-PDC), and highly explosive events generating pumice C-PDC. Effusive and explosive stages sometimes occur during the same eruption, as illustrated by the P1 eruption dated to ~ 1350 AD at Mt Pelée, Martinique, FWI (Boudon and Balcone-Boissard 2021) and the 1530 AD eruption of la Soufrière of Guadeloupe (Boudon et al. 2008). In some rare cases, flank collapse following

Published online: 18 February 2025

the growth of a lava cryptodome in one flank of the volcano can trigger laterally directed blasts that generate extensive high-energy diluted pyroclastic density currents (D-PDC), as illustrated for instance by the 1980 eruption at Mt St Helens, WA, USA (Voight et al. 1981) and the 1956 Bezymianny eruption, Kamchatka, Russia (Belousov 1996; Belousov et al. 2007). Several eruptions show the sequence of flank collapse, laterally directed blast, Plinian column, and/or deposition of pumice C-PDC, terminated by lava dome growth, such as the 1980 eruption at Mt St Helens (Voight et al. 1981) and the 1956 Bezymianny eruption (Belousov 1996; Belousov et al. 2007). At Mt St Helens in 1980, the combination of direct observations of the eruption with the study of the erupted products allowed major advances in the understanding of the volcanic processes. A better understanding of these devastating eruptions is necessary to progress towards a better evaluation of the risk assessment, which is particularly important for densely populated areas.

Although located in a remote area with limited risks of casualties, Bezymianny's 1956 climactic eruption is an opportunity to investigate the mechanisms and timescales that lead to flank collapses and laterally directed blast explosions, pumiceous explosive phases, and lava dome growths, which can be used for other volcanic systems for which risk assessment is highly critical. To this aim, we propose two companion papers: the present one (part I) is dedicated to a refinement of the plumbing system beneath Bezymianny's edifice through petrological constraints, and the second one (part II; Ostorero et al. in press) focuses on the timescales of the reactivation processes before Bezymianny's 1956 climactic eruption.

The 1956 eruption of Bezymianny volcano

Geological setting

Bezymianny is an andesitic stratovolcano located in the Central Kamchatka Depression that results from the Pacific oceanic plate subducting beneath the Okhotsk oceanic plate at a rate of 8 cm/year (DeMets 1992). Bezymianny belongs to the Klyuchevskoy group of volcanoes that includes the presently active Bezymianny, Tolbachik, and Klyuchevskoy volcanoes (with approximate altitudes of 2900, 3700, and 4700 m, respectively). Yet, these three volcanoes have different compositions, eruptive styles, and feeding systems, as demonstrated by seismic tomography (Koulakov et al. 2017). Indeed, seismic tomography and thermal remote sensing studies suggested that the explosive Bezymianny volcano is fed through a dispersed system of crustal reservoirs, where felsic magma fractionates from mafic magma bodies, ascending to the upper crust from where eruptions of andesitic magmas are sourced (Koulakov et al. 2017, 2021; Coppola et al. 2021).

Eruptive chronology

After 1000 years of dormancy, Bezymianny awakened in September 1955 with increasing seismic activity (hypocenters estimated at a depth less than 5 km; Gorshkov and Bogoyavlenskaya 1965; Belousov et al. 2007). On October 22, 1955, the first historical eruption of Bezymianny began with an explosive phreatic emission of steam and ash (Gorshkov 1959), followed by lava dome growth in the new crater (seen for the first time on 25 January 1956) and slow uplift (~ 100 m) of the southeastern slope of the cone interpreted as magma emplacement in a form of a cryptodome (Belousov and Belousova 1998). The volume of the accumulated cryptodome magma was estimated to be 0.15–0.20 km^3 (Belousov et al. 2007). On 30 March 1956, the flank of the Bezymianny cone, destabilized by the intrusion of a cryptodome, gravitationally collapsed. This collapse produced a debris avalanche with a volume of 0.5 km^3, followed by a laterally directed blast (hereafter referred to as the blast) with a volume of 0.2–0.4 km^3, resulting from the depressurization of the cryptodome. The blast led to formation of a devastating D-PDC that covered an area of ~ 500 km^2 (Belousov and Belousova 1998; Belousov et al. 2007; Fig. 1a). The depressurization of the cryptodome, and progressively of the conduit-magma reservoir feeding system, induced by the edifice collapse led to eruption of the blast D-PDC and the post-blast pumice C-PDC generated by an eruptive cloud of 30–40 km high that immediately collapsed gravitationally into widespread pumiceous C-PDCs totaling 0.5 km^3 DRE (Belousov 1996; Turner et al. 2013). The total volume of emitted magma during the climactic phase of the eruption was on the order of 1 km^3 DRE (Belousov 1996). The 1956 eruption was followed by still active intermittent lava dome growth and periodic collapses into block-and-ash C-PDCs (Turner et al. 2013; Davydova et al. 2022). Since 1977, there have been a few explosive eruptions almost every year, making Bezymianny one of the most active volcanoes in the world since 1956.

Petrology of the erupted products

The 1956 erupted materials are calc-alkaline andesites (60–62 wt% SiO_2, 18–19 wt% Al_2O_3, 6–7 wt% CaO, 3–4 wt% Na_2O, and 1–2 wt% K_2O; Belousov 1996; Neill et al. 2010; Shcherbakov et al. 2013; Davydova et al. 2022) making up two lithologies differing in (i) their vesicularity, with the clasts from the blast being on average less vesiculated than the pumices from the post-blast C-PDCs (Belousov et al. 2007) (Fig. 1b–c), and (ii) the crystallinity of the groundmasses, with the clasts from the blast being more

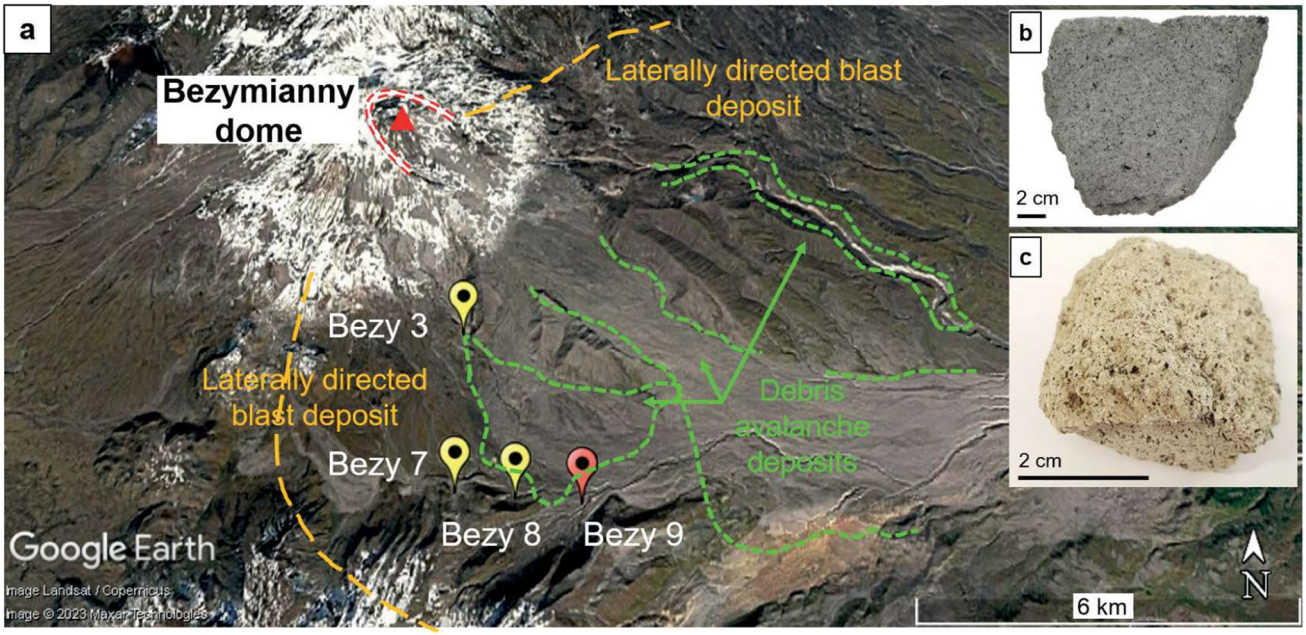

Fig. 1 Bezymianny volcano with its main surface features, sample location, and main sample types. **a** Bezymianny edifice showing the scar of the 1956 flank collapse (red dashed line at the summit), the extent of the deposits from the debris avalanche (yellow dashed lines), and the laterally directed blast on 30 March 1956 (green dashed lines) (Belousov 1996). The sampling sites are marked in orange for the 1956 blast samples (Bezy3, N 55° 56.465′, E 160° 36.887′; Bezy7, N 55° 55.068′, E 160° 36.910′; Bezy8, N 55° 55.066′, E 160° 37.099′) and in red for the post-blast C-PDC pumices (Bezy9, N 55° 54.987′, E 160° 38.843′). Image credit: Google Earth V 7.3.4.8248 (December, 2013), Bezymianny, Kamchatka, N 55° 57.385′, E 160° 39.934′, eye altitude 19.17 km. Image Landsat/Copernicus. Maxar Technologies 2023 [2 March 2023]. **b** Andesite clast from the 1956 cryptodome. **c** Andesite pumice from the 1956 post-blast pumice C-PDC

crystallized than the post-blast C-PDC pumices (Neill et al. 2010). For the blast material, there is a negative correlation between clast vesicularity and groundmass crystallinity (Neill et al. 2010). All juvenile clasts are composed of ~ 35 vol% phenocrysts made up of 21 vol% plagioclase, 3–4 vol% amphibole (partly decomposed), 1–2 vol% Fe-Ti oxides, 1 vol% orthopyroxene, accessory minerals (such as clinopyroxene, Cu-Fe sulfides, and zircon), and ~ 75 vol% groundmass consisting of plagioclase, orthopyroxene, Fe-Ti oxides, silica phases, and a rhyolitic glass (Shcherbakov et al. 2013). Amphibole has a bimodal composition (in Al and other elements), where all crystals are surrounded by reaction rims, evidencing a complex magmatic history (Plechov et al. 2008; Shcherbakov et al. 2013; Turner et al. 2013). Plagioclase phenocrysts are strongly zoned, with compositions ranging from 48 to 77 mol% anorthite ($An_{48–77}$; Shcherbakov et al. 2013). Plagioclase microlites from the blast clasts range from An_{30} to An_{50} (Neill et al. 2010), but there are no compositional data for plagioclase from the post-blast C-PDC pumices. Orthopyroxene phenocrysts have homogeneous compositions from 62 to 64 mol% enstatite ($En_{62–64}$; Shcherbakov et al. 2013). Fe-Ti oxides are titanomagnetite and rare ilmenite, with 60–70 mol% magnetite and 20–22 mol% ilmenite ($Mt_{60–70}$ and $Ilm_{20–22}$, respectively; Shcherbakov et al. 2013). Silica phases are ubiquitous in the post-blast C-PDC pumices and in the blast samples (Gorshkov and Bogoyavlenskaya 1965; Plechov et al. 2008). Glasses are rhyolitic, with matrix glasses showing SiO_2 contents from 74 to 79 wt% and plagioclase-hosted melt inclusions showing 73–76 wt% SiO_2 (Shcherbakov et al. 2013). From bulk H_2O measurements (Karl-Fischer titration) and mass balance calculations for the blast samples, Neill et al. (2010) suggested glass H_2O contents of up to 2 wt% in the less vesiculated clasts (density > 2000 kg/m^3) and of about 1.0 ± 0.5 wt% in the more vesiculated material, which indicates solubility pressures of 10–20 MPa.

The magma plumbing system prior to the 1956 and recent eruptions

Numerous studies have attempted to estimate the conditions of magma storage prior to the 1956 eruption, and have generally proposed the existence of two distinct reservoirs. However, depths, pressures, and temperatures vary from study to study. Using phenocryst compositions, Kadik et al. (1986) estimated a deep reservoir at pressures of 300–800 MPa (depths of 11–30 km recalculated with a rock density of 2700 kg/m^3), temperatures of 875–930 °C, and > 6 wt% H_2O

dissolved in the melt. Plechov et al. (2008) also inferred a magma storage pressure range of 300–800 MPa calculated using the MELTS algorithm (Ghiorso and Sack 1995) and a temperature of 890 ± 20 °C calculated from amphibole-plagioclase thermometry. These authors interpreted the amphibole breakdown at depths of > 500 MPa as to have resulted from a re-heating to ~ 1005 °C prior to eruption. Constraints from phase-equilibrium experiments by Almeev et al. (2013a, b) equally suggested magma storage and partial crystallization at a pressure of ~ 600 MPa (23 km depth) and temperatures of 800–920 °C. Shcherbakov et al. (2013) suggested a deep reservoir, in which amphibole and plagioclase were stable, at ≥ 200 MPa (≥ 8 km depth), but at a relatively low temperature of < 850 °C determined based on phase equilibrium experiments at H_2O-saturated and CO_2-free conditions. There is thus consensus for the existence of a deep reservoir, in which amphibole was stable, at pressures of about ≥ 200 MPa (~ 8 km) and possibly up to 800 MPa (~ 30 km) and temperatures between ~ 775 and 930 °C.

A shallower reservoir has also been proposed from amphibole destabilization rims and phase-equilibrium experiments starting with the 1956 eruption products (Shcherbakov et al. 2013). These authors suggested that magma of the climactic phase of the 1956 eruption was transiently stored at a pressure of 50–100 MPa (~ 2–4 km depth) and at a temperature of 890–930 °C for at least up to 40 days in the case of the cryptodome-forming and possibly as short as 2–14 days for the pumice-forming magma. The authors further suggested heating of the magma upon final ascent to ~ 950–1000 °C, likely from latent heat release resulting from decompression-induced microlite crystallization. Our results meet the authors' interpretation of the existence of a shallow pre-eruptive reservoir, in which amphibole was not stable, at pressures somewhere between 30 and 100 MPa (1–4 km) and at magma temperatures of ~ 900–930 °C.

Although the post-1956 eruptions mostly produced basaltic andesites (as opposed to andesites in 1956) and the magmas may not be stored at the conditions they were stored in 1956, recent seismic surveys suggest the existence of two levels of magma storage. From seismic tomography surveys below the Klyuchevskoy group of volcanoes, Thelen et al. (2010) and Fedotov et al. (2010) suggested a large and deep magma body at ≥ 7–10 km depth, that is at pressures of ≥ 200–300 MPa, for the 1956–2010 period of Bezymianny activity. From earthquake distribution centers, Thelen et al. (2010) also proposed magma storage at 1.0–1.5 km depth, that is, at ~ 30–40 MPa. Combining seismic tomography, remote sensing, and petrological data, Koulakov et al. (2021) suggested that Bezymianny's 2017 explosive eruption was controlled by the coexistence of magma and gas reservoirs located at depths of 2–3 km below the summit.

Characterizing the plumbing system beneath Bezymianny prior to 1956 is a prerequisite step for unravelling the processes and components driving Bezymianny's eruptive dynamics and the basis for constraining the timescales of the reactivation processes before the 1956 eruption (Ostorero et al. in press). While several estimates exist, our study builds upon them by petrologically characterizing a larger number of blast and pumice samples and examining a greater number of phases in more detail. To refine the pressure (depth) and temperature conditions of the shallow to deep plumbing system beneath Bezymianny, we have performed a petrological study of the 1956 blast products and post-blast C-PDC pumices, with key constraints from amphibole destabilization rims and groundmass microlites, as well as melt inclusion oxide and volatile concentrations and amphibole compositions. The proposed 1956 magma plumbing system beneath Bezymianny is then compared to the recent plumbing system beneath the volcano as well as other volcanic centers that have experienced sector collapse that generated a blast followed by a pumiceous explosive phase.

Methods

Field sampling

More than 250 samples were collected at four main localities (Bezy3, Bezy7, Bez8, Bezy9) from the deposits of the laterally directed blast and the post-blast pumiceous C-PDCs, during a 3-week field mission in Kamchatka in August 2019 (sample localities in Fig. 1a), of which a subset was studied in detail (Table 1). The samples from the Bezy3 locality are blocks from the proximal deposit of the blast (~ 3 km from the summit). The samples from the Bezy7 and Bezy8 localities come from a trench dug in the same deposit at ~ 6 km away from the summit, which contained several clasts of variable vesicularity. The samples from the Bezy9 locality are pumices from the post-blast C-PDCs.

Clast density vesicularity measurements

Bulk densities were obtained on a series of clasts from the localities of Bezy3, Bezy7 (about 100 clasts), and Bezy9 (about 124 clasts), by weighing 1-cm-wide fragments in air and in water (Archimede's principle), previously immersed in a paraffin bath to avoid water penetration into the vesicles. The bulk vesicularity (Φ_b) was then obtained from the fragment weight in air and water, using a DRE density of 2650 kg/m^3 (Kadik et al. 1986).

Textural analysis

Eighteen samples with variable vesicularity were selected for detailed study, mounted in epoxy resin, and polished for a petrological study. Sample observation was performed using a

Table 1 Sample description and textures of the 1956 erupted products

Eruption type	Sample no.[a]	Lithology	Φ^b (vol%)	Type of Amph rim[c]	Silica phase	Plag microlites[d]	
						Φ_{Plag} (vol%)	logN_{Plag} (m^2)
Blast	Bezy3b-17	Vesiculated clast	35.5	*nd*	*nd*	42.7	12.52
	Bezy3e	Vesiculated clast	*nd*	1 to 2	Qtz + Crs	*nd*	*nd*
	Bezy7a-64	Very dense clast	8.7	*nd*	*nd*	*nd*	*nd*
	Bezy7a-66	Dense clast	24.0	2	Crs	*nd*	*nd*
	Bezy7a-67	Vesiculated clast	41.4	1 to 2	Qtz + Crs	*nd*	*nd*
	Bezy7a-70	Pumice	48.7	1	Qtz	33.3	11.82
	Bezy7a-84	Vesiculated clast	36.4	2	Crs	36.8	11.86
	Bezy7a-86	Dense clast	32.0	2	Crs	33.2	12.86
	Bezy7b-8	Pumice	*nd*	1	Qtz	*nd*	*nd*
	Bezy7b-13	Vesiculated clast	42.4	1 to 2	Qtz + Crs	25.0	11.97
	Bezy8b	Dense clast	*nd*	2	Crs	*nd*	*nd*
C-PDC	Bezy9-124a	Pumice	38.6	*nd*	*nd*	35.6	11.77
	Bezy9-124b	Pumice	38.6	*nd*	*nd*	29.8	11.87
	Bezy9-17	Pumice	46.0	1	Qtz	31.8	11.87
	Bezy9-18	Pumice	45.7	*nd*	*nd*	*nd*	*nd*
	Bezy9-100	Pumice	57.9	*nd*	*nd*	*nd*	*nd*
	Bezy9-101	Pumice	54.4	*nd*	*nd*	*nd*	*nd*
	Bezy9-107	Pumice	63.2	1	Qtz	*nd*	*nd*

nd for not determined; Amph, Plag, Qtz, and Crs for amphibole, plagioclase, quartz, and cristobalite, respectively

[a]Clasts from samples Bezy3, Bezy7, Bezy8, and Bezy9 selected on their vesicularity (locations given in Fig. 1)

[b]Bulk area contents recalculated on a bubble-free basis

[c]Amphibole Type-1 and Type-2 end-members and intermediate types (types 1 to 2)

[d]Area content and number density of the plagioclase microlites recalculated on a bubble-free basis

scanning electron microscope (SEM; Merlin Compact ZEISS at ISTO, Zeiss Supra 55VP at ISTeP, and Carl Zeiss EVO MA10 at the PARI platform, IPGP). The backscattered scanning electron (BSE) images served first to select representative zones for the textural analysis of the groundmasses and the decomposition rims around amphiboles (10–30 representative crystals per sample/polished section), and second, to guide analyses by electron microprobe.

For the groundmass characterization, the selected BSE images were processed using the SPO software (Launeau and Robin 1996), following the method described in Martel and Poussineau (2007). The matrix plagioclase area percentage (Φ_{Plag}) and the area number density of matrix plagioclase (N_{Plag}) was determined as follows:

$$\Phi_{Plag} = (\text{plagioclase microlite area}/\text{bubble} - \text{free matrix area}) \times 100$$

$$N_{Plag} = \text{number of matrix plagioclase}/\text{bubble} - \text{free matrix area}$$

Chemical analyses

Whole-rock analyses were performed by wet chemistry, using an inductively coupled plasma optical emission spectrometer (ICP-OES; Centre de Recherches Pétrographiques et Géochimiques, CRPG, Nancy, France), as described in Ostorero (2022). Oxides that were characterized are SiO_2, TiO_2, Al_2O_3, Fe_2O_3, MnO, MgO, CaO, Na_2O, K_2O, and P_2O_5. Internal standards from CRPG were used for calibration and the errors are of < 10% for SiO_2, < 20% for K_2O and TiO_2, and < 15% for the other oxides.

The compositions of the crystals and glasses were obtained using electron microprobes (EMP; Cameca SX Five at ISTO, JEOL JXA-IHP-200F from the platform MACLE-CVL, Orléans, or CAMECA SX-Five and SX-100 from Service Camparis, Paris).

Amphibole phenocrysts, amphibole rim microlites, matrix microlites, and silica polymorphs were analyzed using both EMPs at Orléans. Amphibole phenocrysts, amphibole rim microlites, and matrix microlites were analyzed at an acceleration voltage of 15 kV, a beam current of 10 nA, and a focused beam. Silica polymorphs were analyzed at an acceleration voltage of 15 kV, a beam current of 6 nA, and a slightly defocused beam (spot size of 2 µm). For all elements, peak and background counting times were set to 10 and 5 s, respectively. Calibration standards were albite, andradite, orthoclase, pyrophanite, corundum, magnetite, magnesium, topaz, and vanadinite. The analytical errors on

the oxide analyses are 1% relative for SiO_2 and Al_2O_3, 2% for CaO, 3% for FeO, MgO, and TiO_2, and 5% for MnO, Na_2O, and K_2O.

The melt inclusions were analyzed using the Camparis EMP. To ensure that only melt inclusions with minimal post-entrapment modification were analyzed, we selected melt inclusions with round shape free of visible daughter crystals and bubbles (possibly indicating outgassing), as recommended in Balcone-Boissard et al. (2018) or Rose-Koga et al. (2021). Analyses were performed following the methodology developed by Balcone-Boissard et al. (2018) with an acceleration voltage of 15 keV, a beam current of 10 nA for major elements and of 80 nA for F and Cl, and a defocused beam of 6–10 µm (d'Augustin 2021; Ostorero 2022). Counting time was set to 10 s for major elements, 120 s for F, and 60 s for Cl, and Na was analyzed first to minimize loss by volatilization under the electron beam. Internal standards from Balcone-Boissard et al. (2018) used for glass measurements intercalibration EMP sessions were analyzed at the same conditions as the melt inclusions. For comparison with literature data, the glass analyses are reported with all Fe converted to FeO and normalized without considering MnO and P_2O_5 (both < 0.2 wt%). Post-entrapment corrections were calculated from the EMP analyses of the melt inclusions in orthopyroxene and plagioclase (not assessed for amphibole and magnetite), based on the Fe–Mg and Na-Ca partition coefficients, respectively, using the equations of Putirka (2008). The calculations suggested that post-entrapment crystallization was < 3% for melt inclusions hosted by both minerals, so that we kept the raw EMP values (reported in SM1).

The minerals were analyzed using the Camparis EMP, with counting times on peak and background set at 80 s for Fe and Mg (for orthopyroxene), and 10 s for the other elements. Calibration standards were albite, andradite, orthoclase, pyrophanite, corundum, magnetite, and magnesium oxide. Typical analytical errors on major elements are ~ 1% relative for SiO_2, Al_2O_3, and CaO, 3% for FeO, MgO, and TiO_2, and 5% for Na_2O, K_2O, and MnO.

Identification of the silica polymorphs (quartz, cristobalite, tridymite) was performed following the procedure described in Martel et al. (2021b), consisting of characterizing the nature of the silica polymorph both, by Raman spectroscopy (using a Renishaw InVia spectrometer at a wavelength of 514 nm and a maximum power of 100mW; BRGM-ISTO, Orléans, France) and by EMP (Orléans). This allows identification as a function of the silica phase composition: quartz is almost pure SiO_2 whereas tridymite and cristobalite contain about 2–4 wt% of other components such as Al_2O_3 and alkalis (Martel et al. 2021a, b; Davydova et al. 2022).

Analyses of H_2O and CO_2 dissolved in the glasses

The H_2O and CO_2 contents of the glasses, either melt inclusions or residual glasses, were measured using a secondary ion mass spectrometer (SIMS; IMS 1280 HR2 spectrometer at the Centre de Recherches Pétrographiques et Géochimiques, CRPG, Nancy), following the methodology of Bouvier et al. (2010), as described in d'Augustin (2021). The calibration curve for H_2O was calculated using best-fit regressions in $[H_2O]$ versus $^{16}OH/^{18}O$ using secondary standards from Shishkina et al. (2010). The regression curve was fitted for H_2O by a polynomial regression and for CO_2 by a linear regression. The mean standard deviation for H_2O measurements is 125 ppm and 43 ppm for CO_2.

Thermobarometric and hygrometric constraints

To constrain quantitatively crystallization conditions during magma storage, we have used the compositions of amphibole phenocrysts and of magnetite-ilmenite pairs (from amphibole decomposition rims) and melt inclusions.

From amphibole compositions, crystallization temperature and pressure were calculated using the calibrations of Higgins et al. (2022), and crystallization temperature, pressure, and melt H_2O concentration were calculated using the Ridolfi (2021) calibrations, which are slightly modified from the calibrations of Ridolfi and Renzulli (2012) (Fig. 7; SM2). As detailed in the supplementary text, we have tested the performance of the two calibrations on experimental amphibole compositions equilibrated at known conditions. The main findings are (1) that the Higgins et al. (2022) calibration provides more precise temperature and pressure estimates than the Ridolfi (2021) calibration (SM3_Fig. 1a–d); (2) that the Ridolfi (2021) calibration provides rough estimates on melt H_2O concentration and tends to underestimate melt H_2O concentrations at more than ~ 6 wt% (SM3_Fig. 1e); and (3) that the Ridolfi (2021) calibration provides extremely rough estimates on oxygen fugacity (fO_2) and tends to overestimate fO_2 at reducing conditions and underestimate fO_2 at oxidizing conditions (SM3_Fig. 1e). Temperature and pressure calculated with the Higgins et al. (2022) calibrations are nearly always within the uncertainty of the experimental test data (outside the uncertainty in only ~ 20% and 10% of the cases). Temperature, pressure, fO_2, and melt H_2O concentration calculated with the Ridolfi (2021) calibrations in contrast commonly deviate from the known experimental values by more than the estimated uncertainty (in ~ 60%, ~ 70%, ~ 80%, and ~ 50% of the cases). The compositions of the analyzed Bezymianny amphiboles fall within the range of amphibole compositions of both the Higgins et al. (2022) ($n = 409$) and the

Ridolfi (2021) ($n = 72$) calibration datasets for all oxide concentrations (SM2). Both calibrations are therefore applicable to our dataset, but given the higher precision and realistic uncertainty estimates of the Higgins et al. (2022) thermobarometer, we report only these estimates in the main text, supplemented by fO_2 and melt H_2O concentrations calculated using the Ridolfi (2021) calibrations. Temperatures and pressures calculated with the Ridolfi (2021) thermobarometers are reported in the supplementary Table SM2_AmphCalc for comparison. Within the results section, we present uncertainties as given by Ridolfi (2021) and Higgins et al. (2022), but highlight that the uncertainties provided by Ridolfi (2021) are commonly underestimates, and that maximum uncertainties may be larger than the indicated errors (for details, see text in SM3). Magnetite-ilmenite compositional pairs from amphibole decomposition rims were used to calculate pre-eruptive temperatures using the formulation of Sauerzapf et al. (2008).

Equilibrium pressures were calculated from H_2O and CO_2 contents in the melt inclusions using the rhyolitic composition in the VolatileCalc model of Newman and Lowenstern (2022).

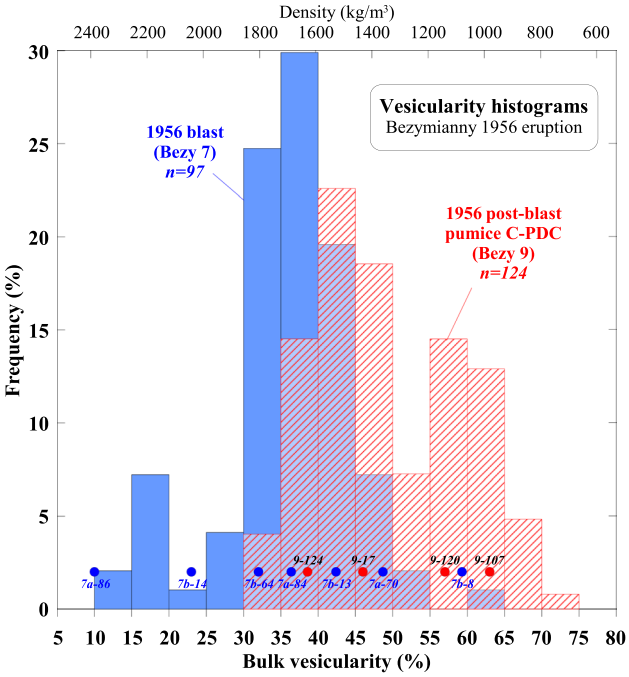

Fig. 2 Frequency histogram of bulk vesicularity for our set of Bezymianny cryptodome and pumice samples (recalculated from sample density using a DRE density of 2650 kg/m.^{3}, as shown by the upper X-axis). Bezy 7 samples from the 1956 blast deposit and Bezy 9 pumices from the post-blast C-PDC deposit are shown in blue and red, respectively. The circles indicate the clasts selected for our detailed petrographic study, labelled with sample names as reported in Table 1

Results

Vesicularity

The frequency histograms of the bulk vesicularities of the blast and the pumiceous C-PDC samples are shown in Fig. 2. The directed blast samples show a range of clast bulk vesicularities from 10 to 60 vol%, with a main mode at 30–45 vol% accompanied by a secondary discrete peak around 15–20 vol% vesicularity. Both vesicularity modes agree with those reported in Belousov et al. (2007), but with opposite relative frequencies. Indeed, we found less than 10% dense material (10–20 vol% porosity) whereas ~ 30% of such material was detected by Belousov et al. (2007), which may reflect the variability of different sampling sites. The present vesicularity distribution and main peak frequency resemble those from the 1980 blast of Mt St Helens (Hoblitt and Harmon 1993).

The post-blast C-PDC pumices show a total range of bulk vesicularities between 30 and 75 vol%, with two main modes at 35–50 vol% and 55–65 vol% vesicularity, which confirms the overall denser character of pumiceous C-PDC deposits compared to Plinian fallout deposits that commonly show a narrow unimodal distribution at bulk vesicularities > 55 vol% (e.g., P1 eruption of Mt Pelée; Martel et al. 2000). The mode at 35–50 vol% vesicularity partially overlaps the one from the blast deposit.

Textures of the amphiboles

Amphibole phenocrysts are euhedral to subhedral and rarely slightly skeletal with sizes of typically < 1–2 mm, but occasionally larger in maximum dimension. All amphibole phenocrysts are partly decomposed, showing reaction rims along grain boundaries, in contact with melt inclusions, or irregularly throughout the crystals. Decomposition rims range from predominantly relatively thin (typically ≤ 15 µm thick) external rims with homogeneous texture (Type-1 rims; Fig. 3a) to relatively thick (typically > 30 µm thick) external rims and pervasive amphibole decomposition with heterogeneous texture (Type-2 rims; Fig. 3b) to intermediate types (referred to as Type-1 to Type-2). C-PDC pumices have predominantly amphibole with Type-1 decomposition rims, but some have amphibole with thin Type-2 decomposition rims. Dense clasts from the blast have amphibole with thick, pervasive Type-2 decomposition rims. Vesiculated clasts from the blast have intermediate Type-1 to Type-2 rims. Amphibole rim type does not vary with amphibole composition.

Thin Type-1 decomposition rims comprise plagioclase, clinopyroxene, orthopyroxene, magnetite, and occasionally ilmenite microlites immersed in ≤ 25 vol% glass. Their

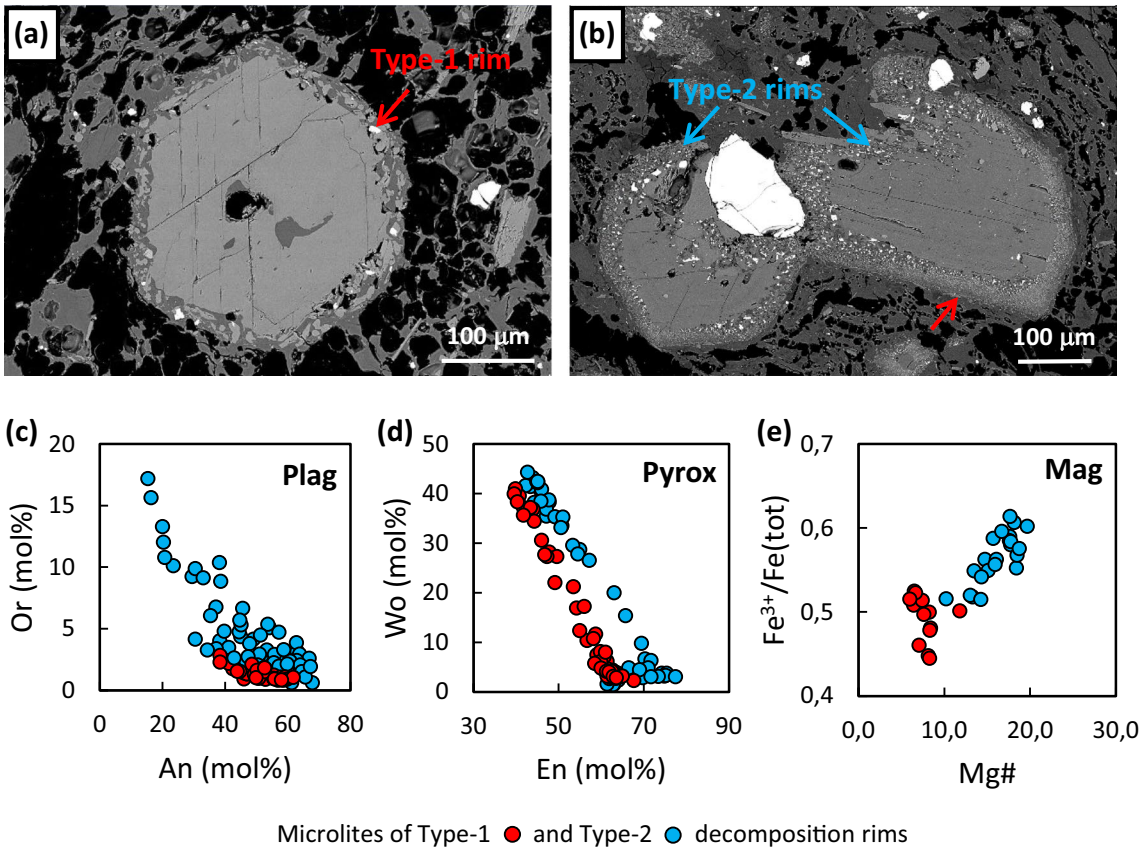

Fig. 3 Amphibole destabilization textures showing end-member types with **a** thin, texturally relatively homogeneous Type-1 decomposition rim in a pumice sample and **b** thick, texturally heterogeneous Type-2 decomposition rim with beginning pervasive decomposition in a dense cryptodome sample. The red arrows indicate Type-1 decomposition rims in amphibole and the blue arrows point to characteristic thick Type-2 decomposition rims. Compositions of microlites in Type-1 and Type-2 amphibole decomposition rims for **c** plagioclase (Plag), **d** pyroxene (Pyrox), and **e** magnetite (Mag). The $Fe^{3+}/Fe(tot)$ composition was calculated based on charge balance. Mg# is the magnesium number calculated as $Mg\# = (\frac{Mg}{Mg+Fe^{2+}} * 100)$

microlites are euhedral to subhedral with sizes of typically ≤ 10–20 µm (Fig. 3a). The Type-2 decomposition rims also comprise plagioclase, clinopyroxene, orthopyroxene, magnetite, and occasionally ilmenite microlites, yet have overall significantly less glass (≤ 5–10 vol%) compared to the Type-1 decomposition rims. Their microlites are euhedral to anhedral, ranging from blocky to skeletal and vermicular with sizes between < < 1 and up to 50 µm (Fig. 3b). Microlite textures and proportions of the outermost layer of the Type-2 decomposition rims (which crystallized first), however, locally compare to those of the Type-1 decomposition rims (Fig. 3b).

Glass composition in the decomposition rims was not analyzed, as the glass pools are generally too small for analysis, but microlites of the Type-1 and Type-2 decomposition rims show characteristic compositional differences. Plagioclase microlites of Type-1 decomposition rims have a limited compositional range and low orthoclase content (~ An_{62-38}, < Or_4), whereas plagioclase microlites of Type-2 rims show a large compositional range (~ An_{68-15}, ~ Or_{1-17}) (Fig. 3c). Pyroxene microlites of Type-1 and Type-2 decomposition rims are enstatite, augite, and pigeonite, where the pyroxenes of Type-2 rims have higher enstatite contents than the pyroxenes of the Type-1 rims (Fig. 3d). Magnetite microlites of Type-1 decomposition rims have low Mg# and low calculated $Fe^{3+}/Fe(tot)$ compared to magnetite crystals of the Type-2 rims (Fig. 3e).

Textures of the groundmass

In both sample types, blast clasts and C-PDC pumices, the groundmass is composed of microlites (< 100 µm in length) of plagioclase, orthopyroxene, clinopyroxene, titanomagnetite, rare apatite, and silica phases (Fig. 4) that are cristobalite and quartz in the blast clasts and only quartz in the C-PDC pumices. The plagioclase microlites form faceted tabular crystals (Fig. 4a). The plagioclase microlite contents are 25–55 vol% in the blast clasts and 30–35 vol% in the C-PDC pumices (Fig. 5a). The areal number density of all plagioclase microlites is about 10^{12} m^{-2} in the pumices and 10^{12-13} m^{-2} in the blast clasts (Fig. 5b).

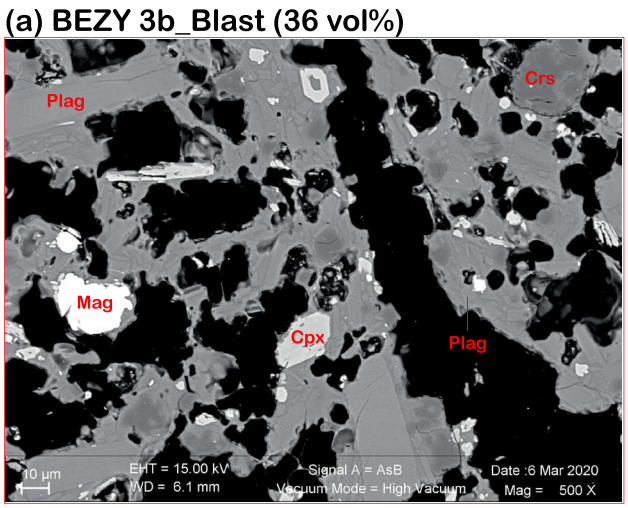

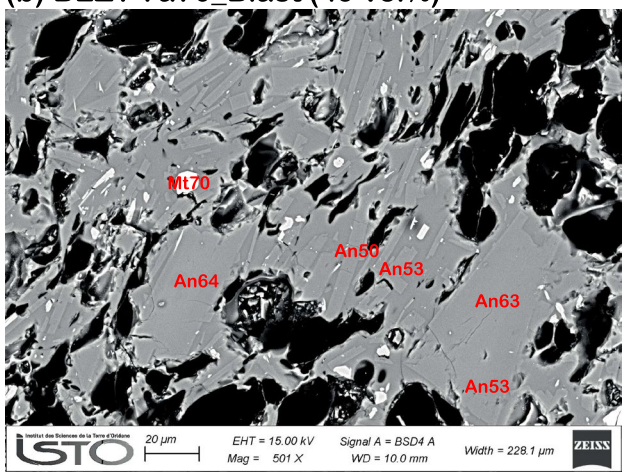

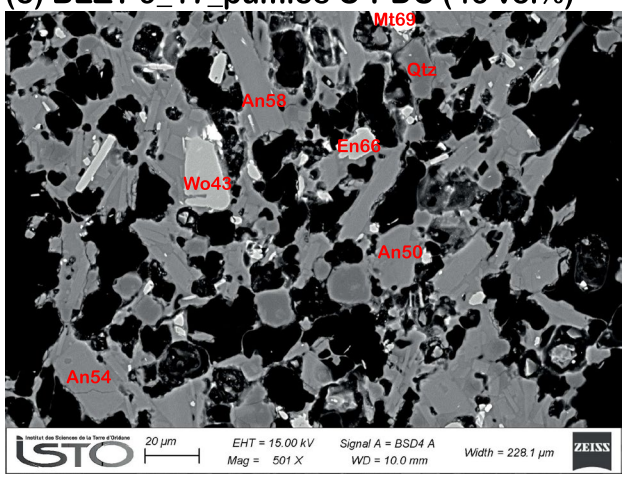

Fig. 4 Backscattered scanning electron microscope images of groundmass characteristics for the 1956 cryptodome and pumice samples. **a** Sample Bezy 3b: moderately vesiculated clast from the cryptodome; **b** sample Bezy 7a: highly vesiculated clast from the blast; and **c** sample Bezy 9_17: pumice from the post-blast C-PDC; *Plag* for plagioclase and *An* gives the anorthite molar content, *Cpx* for clinopyroxene and *Wo* gives the wollastonite molar content, *Opx* for orthopyroxene and *En* gives the enstatite molar content, *Mag* for titanomagnetite and *Mt* gives the magnetite molar content, *Qtz* for quartz, and *Crs* for cristobalite

Whole-rock and phase compositions

The bulk-rock compositions determined in our samples of the 1956 eruption products (Bezy3e and Bezy8f for the blast samples, and Bezy9-18, Bezy9-100, and Bezy9-101 for the post-blast C-PDC pumices; SM1) agree with the compositions determined by Neill et al. (2010) and Shcherbakov et al. (2013), i.e., they are calc-alkaline andesites with no significant compositional differences between the blast and pumiceous C-PDC samples (SM1; Fig. 6).

As previously reported by Turner et al. (2013), we confirm that the 1956 blast and pumiceous C-PDC samples comprise two amphibole populations. Few (~20%) amphibole crystals have low SiO_2 content (< ~42 wt%) and high Al_2O_3 (> ~12 wt%) with magnesio-hastingsite to tschermakitic pargasite composition, while most (~80%) amphibole crystals have high SiO_2 content (> ~42 wt%) and low Al_2O_3 (< ~12 wt%) with tschermakitic pargasite to magnesio-hornblende composition (Fig. 7a; SM2). Intensive parameters calculated from the amphibole compositions (SM2) show similar ranges for the pumice and the blast samples (Fig. 7b–f; SM2). Intensive parameters calculated from amphibole core and rim compositions also show similar ranges (SM2), comprising normally and reversely zoned and largely unzoned crystals (SM2). The main SiO_2-rich amphibole population (~80% of the crystals) mostly calculates a narrow range of crystallization temperatures of ~840–865 °C and a narrow range of crystallization pressures of ~200–300 MPa with relatively small estimated uncertainties of ~ ±6.5–29 (on average ± 16) °C and ~ ± 10–185 (on average ± 55) MPa (Fig. 7b; SM2). Melt H_2O concentrations calculated from the main amphibole population show a limited range ~4.5–6.7 ± 0.8–1.1 (on average ± 0.9) wt%, whereas highly variable fO_2 values are calculated (~ ΔNNO to ~ ΔNNO + 2.6 ± 0.4) (Fig. 7c–d; SM2). The minor SiO_2-poor amphibole population (~20% of the crystals) calculates a relatively large range of and higher crystallization temperatures of ~850–990 °C than the main SiO_2-rich amphibole population, and they also calculate higher crystallization pressures of ~280–700 MPa with relatively large estimated uncertainties of ~ ± 17–50 (on average ± 33) °C and ~ ± 100–240 (on average ± 155) MPa, respectively (Fig. 7b; SM2). Melt H_2O concentrations calculated from the minor amphibole population are higher (~5.4–8.1 ± 0.9–1.4 wt%) than those of the main amphibole population (~4.5–6.7 ± 0.8–1.1), whereas most calculated fO_2 values fall into a narrower range between ~ ΔNNO + 0.9 and ~ ΔNNO + 2.1 (± 0.4) (Fig. 7c–d; SM2). The calculated

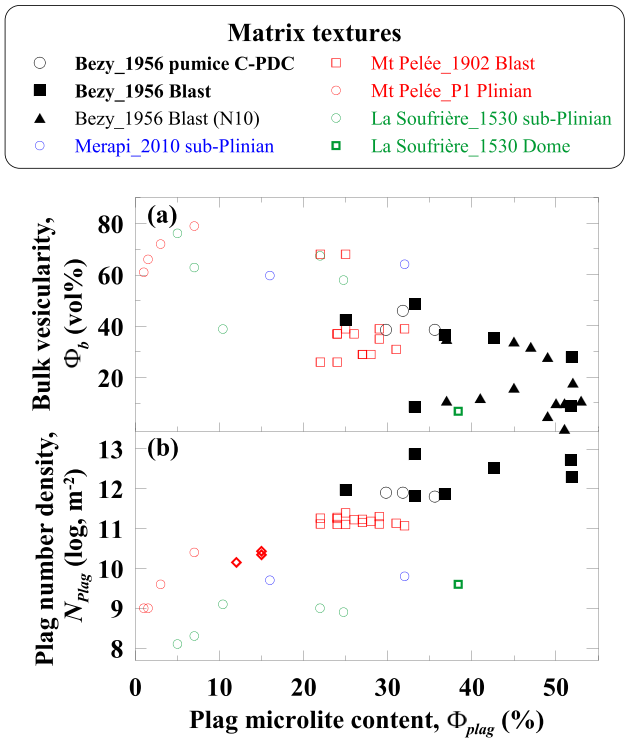

Fig. 5 Quantification of matrix textures defined as the content of matrix plagioclases (microlites and microphenocrysts) as a function of **a** bulk vesicularity, and **b** number density. The plain symbols are cryptodome samples (squares for this study and triangles for Neill et al. 2010) and hollow squares are dome samples. The circles denote pumices from explosive events, with black symbols for the 1956 Bezymianny eruption, blue symbols for the 2010 eruption of Merapi, Indonesia (Preece et al. 2014), red symbols for Mt Pelée (Martel and Poussineau 2007), and green symbols for La Soufrière of Guadeloupe (Martel et al. 2021a)

equilibrium melt compositions are basaltic to rhyolitic, extending from compositions more primitive than the whole-rock composition over approximately whole-rock composition to the composition of the analyzed melt inclusions (Fig. 10). The calculated melt SiO_2 and K_2O concentrations increase, whereas Al_2O_3, TiO_2, FeO, MgO, and CaO decrease with decreasing calculated temperature, pressure, melt H_2O concentration, and fO_2 (Fig. 7e–f; SM2).

The orthopyroxene phenocrysts range from En_{57} to En_{68} composition (enstatite mol%; Fig. 8) and are commonly multiply zoned crystals with generally normal and rare reverse zonings that are detailed in the companion paper dedicated to the reactivation timescales (Ostorero et al. in press). The orthopyroxene microlites in the blast clasts and the C-PDC pumices are $En_{63–68}$ (Fig. 8). Clinopyroxene microlites were only found in the blast clasts and are $Wo_{40–43}$ (wollastonite mol%; SM1).

The plagioclase microlites from the C-PDC pumices range from $An_{49}Or_{1.8}$ to $An_{65}Or_{0.2}$ and those from the blast clasts range from $An_{36}Or_{4.5}$ to $An_{77}Or_{0.2}$ (Fig. 9). In both sample types, the largest microlites are zoned, with cores > An_{60} and rims mostly < ~ $An_{50–60}$. The microlites in the blast clasts are slightly enriched in Or (by ~ 1 mol%) and extend towards more albitic compositions ($An_{36–46}$) with respect to those from the C-PDC pumices.

The titanomagnetite microlites are $Mt_{69–71}$ with TiO_2 contents of 9–10 wt% (SM1). No ilmenite was detected as microlites in the groundmass, but few ilmenites were found in the amphibole decomposition rims. Should magnetite and ilmenite from the amphibole rims be in equilibrium, the temperatures calculated using the formulation of Sauerzapf et al. (2008) give temperatures from 860 to 910 °C, and thus temperatures at the high end of temperatures calculated for the main (SiO_2-rich) population (~ 845–865 ± 6.5–29 °C) and temperatures at the low end of temperatures calculated for the minor (SiO_2-poor) amphibole population (~ 850–990 ± 17–50 °C).

Silica polymorphs form quartz in the C-PDC pumices and coexisting quartz and cristobalite in the blast clasts (Fig. 4a). No tridymite was identified in the 1956 samples (but is present in the recent Bezymianny lavas; Davydova et al. 2022).

Melt inclusions are rhyolitic, with SiO_2 contents ranging from 73 to 80 wt% (Fig. 6). There is no significant compositional difference between the melt inclusions from the 1956 blast samples (Shcherbakov et al. 2013 and this study) and from the C-PDC pumices, either trapped in orthopyroxene or plagioclase. Yet, the melt inclusions show a differentiation trend depending on their host minerals: they are increasingly differentiated (increasing SiO_2 with decreasing Al_2O_3 contents) from amphibole over orthopyroxene, to apatite (Fig. 6). The detected melt inclusion composition in titanomagnetite is enriched in FeO (by more than 1 wt%) and depleted in alkalis with respect to those trapped in other minerals, which suggests mineral-melt interactions that conceal the melt composition at the time of entrapment or matrix contamination of EMP analyses.

The residual matrix glasses of both blast and pumice samples show a narrow range of compositions with SiO_2 contents of 74–80 wt% SiO_2 and K_2O contents of 3–6 wt% (Neill et al. 2010; Shcherbakov et al. 2013; Fig. 6).

Volatile contents

Few melt inclusions in the phenocrysts from the C-PDC pumices were large enough for volatile analysis using SIMS. They show large ranges and of contents, from 0.5 to 7.8 wt% H_2O and 0 to 1700 ppm CO_2 (Fig. 10). The melt inclusions in amphiboles are relatively poor in CO_2 (< 300 ppm) and have H_2O contents from ~ 4 to 8 wt%, suggesting equilibration pressures from ~ 150 to 350 MPa (assuming a temperature of 900 °C; Newman and Lowenstern 2022). The melt inclusions in orthopyroxene have CO_2 contents from 500 to 1700 ppm and H_2O contents mostly around 4 wt%, in

agreement with equilibration pressures of ~ 200 to 350 MPa. The melt inclusions in plagioclase and titanomagnetite have lower CO_2 contents (< 250 ppm) and H_2O contents around 2.5 and 4.0 wt%, suggesting saturation pressures from about 75 to 150 MPa at 900 °C (Fig. 10). Since there is no clear evidence of volatile saturation at the time of melt entrapment, these pressures may be considered as minimum values.

Discussion

The deep reservoir

The intensive parameters of the deep reservoir beneath Bezymianny may be refined by the glass volatile contents and the phenocryst compositions (mostly amphiboles) of the 1956 samples, as follows. The SIMS measurements in the orthopyroxene-hosted melt inclusions show a CO_2 degassing trend (from ~ 1500 to 750 ppm at constant ~ 4.0 ± 0.5 wt% H_2O) following decompression from ~ 350 to 200 MPa (Fig. 10). Whereas melt inclusions in other phenocrysts, such as plagioclases and magnetites, show H_2O contents comparable to those in pyroxenes, the amphibole-hosted melt inclusions have H_2O contents from ~ 5.0 to 8.0 wt%. All amphibole phenocrysts of a specific sample have decomposition rims of the same type, suggesting that the crystals have the same origin. Given that the amphibole phenocrysts calculate melt compositions that encompass bulk rock and that extend to melt inclusion compositions, we interpret them as phenocrysts crystallized from the 1956 Bezymianny magma at a range of conditions. We infer that the calculated crystallization pressures of 200–700 ± 10–250 MPa, melt H_2O concentrations of ~ 4.5–8.1 ± 0.8–1.4 wt%, and temperatures of ~ 840–990 ± 6.5–50 °C (Fig. 7b–c; SM2) are largely realistic estimates within the given uncertainties. The main amphibole population calculates conditions between ~ 200 and 300 ~ ± 55 MPa, ~ 840–865 ~ ± 16 °C, and melt H_2O concentrations of ~ 4.5–6.7 ~ ± 0.9 wt%. Considering the uncertainties, we interpret the calculated values to record crystallization over a narrow pressure interval near 250 MPa, from a magma with largely homogeneous temperature (~ 850 °C) and largely homogeneous melt H_2O concentration (~ 5.0 wt%). The minor amphibole population in contrast calculates pressures between ~ 280 and 700 ~ ± 155 MPa at temperatures of ~ 850–990 ~ ± 33 °C and melt H_2O concentrations of ~ 5.4–8.2 ≥ ± 1.2 wt%. Considering the uncertainties, we interpret the calculated values to record crystallization below the storage zone of the resident magma (at ≥ 280 MPa), possibly from magma with slight variations in temperature (~ 880–960 °C) and melt H_2O concentration (~ ≥ 6.0 wt%). Therefore, the melt volatile contents from orthopyroxene-hosted inclusions and the intensive parameters calculated from amphibole compositions indicate a deep reservoir whose upper part was at a pressure of ~ 200–350 ~ ± 55 MPa with melt H_2O concentrations of ~ 4–5 ~ ± 0.9 wt% and a temperature of ~ 840–865 ~ ± 16 °C (Fig. 12). Yet, the minor SiO_2-poor amphibole population indicates crystallization at higher pressures of ~ 280–700 ~ ± 155 MPa, temperatures of ~ 850–990 ~ ± 33 °C, and melt H_2O concentrations of ~ 5.4–8.1 ~ ± 1.2 wt%, which we consider as largely realistic estimates within the uncertainties, but which could be underestimated for melt H_2O concentration (cf. SM3). In combination with amphibole-bearing melt inclusions with H_2O contents > 4.5 wt%, and up to 8.0 wt%, the amphibole compositions suggest that the deep reservoir extended to ~ > 300 MPa. Magma contributing to the 1956 eruption was thus assembled over a significant depth range, which likely degassed a significant range of melt H_2O concentrations (~ 4.0 to ~ 8.0 wt%) upon ascent and shortly prior to eruption. Most likely, the lower part of the deep reservoir was CO_2-rich like the shallower part, but melt inclusions of such composition were not detected, and we therefore cannot exclude the possibility that a H_2O-rich CO_2-poor (< 250 ppm) magma reservoir existed (from which amphibole with the H_2O-rich inclusions derived) (Fig. 10). In either case, the large range of H_2O contents in amphibole-hosted melt inclusions, combined with a large differentiation trend defined by the melt compositions calculated from amphibole chemometry (from more primitive than bulk-rock to melt-inclusion compositions; Fig. 6), suggests that amphibole crystallized over a significant range of melt compositions, H_2O contents, and pressures. Pre-eruptive recharge of relatively cold magmas in the upper part of the deep reservoir (~ 840–865 °C) by relatively hot magmas from the lower part of the deep reservoir (~ 850–990 °C) will have modulated their temperatures to intermediate ones like those (~ 860–910 °C) estimated from magnetite-ilmenite pairs in amphibole breakdown rims. Overall, our results concur with previous findings of a deep reservoir where partial crystallization took place at pressures of ≥ 200 MPa and temperatures of ≥ 850 °C (Kadik et al. 1986; Plechov et al. 2008; Almeev et al. 2013a, b; Shcherbakov et al. 2013), but we provide more robust pressure and temperature constraints and new insights on the range of volatile concentrations in this reservoir. The fO_2 within the deep reservoir, however, remains largely unconstrained at ~ NNO to NNO + 2.9 ± 2.0 (Fig. 7d; SM2).

To summarize, we propose a deep reservoir in which magma mostly crystallized at pressures of ≥ 200–350 MPa to ≤ 700 MPa (i.e., ≥ 7.5–13 to ≤ 26 km depth), temperatures of ~ 840–990 °C, melt H_2O contents of ~ 4.0–8.0 wt%, and CO_2 contents up to 1500 ppm (Fig. 12).

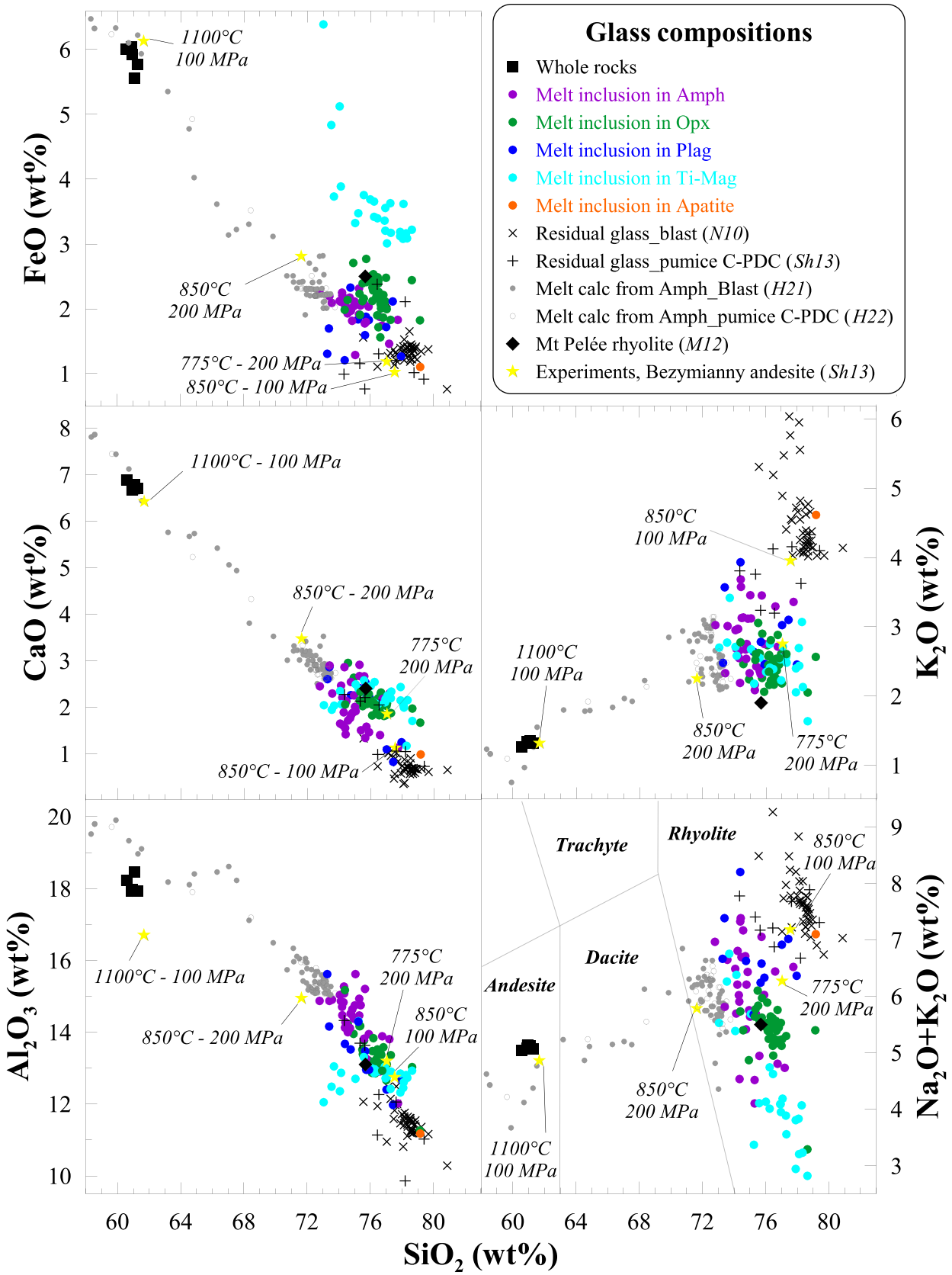
Glass compositions
Whole rocks
Melt inclusion in Amph
Melt inclusion in Opx
Melt inclusion in Plag
Melt inclusion in Ti-Mag
Melt inclusion in Apatite
Residual glass_blast (N10)
Residual glass_pumice C-PDC (Sh13)
Melt calc from Amph_Blast (H21)
Melt calc from Amph_pumice C-PDC (H22)
Mt Pelée rhyolite (M12)
Experiments, Bezymianny andesite (Sh13)
FeO (wt%)
CaO (wt%)
K2O (wt%)
Al2O3 (wt%)
Na2O+K2O (wt%)
SiO2 (wt%)
1100°C 100 MPa
850°C 200 MPa
775°C - 200 MPa
850°C - 100 MPa
1100°C - 100 MPa
850°C - 200 MPa
775°C 200 MPa
850°C - 100 MPa
850°C 100 MPa
1100°C 100 MPa
850°C 200 MPa
775°C 200 MPa
1100°C - 100 MPa
775°C 200 MPa
850°C - 200 MPa
850°C 100 MPa
Trachyte
Rhyolite
Andesite
Dacite
850°C 100 MPa
775°C 200 MPa
850°C 200 MPa
1100°C 100 MPa

◂**Fig. 6** Selected Harker diagrams showing the compositions of Bezymianny (BZ) whole rocks, melt inclusions (trapped in amphibole, plagioclase, orthopyroxene, titanomagnetite, and apatite), and residual glasses. The data come from Neill et al. (2010) (*N10*), Shcherbakov et al. (2013) (*Sh13*), and this study. Glass compositions from selected experiments performed by Shcherbakov et al. (2013) using the Bezymianny 1956 andesite as starting material are reported (pressure–temperature conditions only labelled in two diagrams for clarity); note that the run at 775 °C and 200 MPa best approaches the pre-eruptive conditions according to Shcherbakov et al. (2013). The melt compositions calculated from amphibole compositions after Higgins et al. (2022) (*H22*) are reported to compare to the natural trend of Bezymianny residual glasses. The composition of Mt Pelée rhyolitic glass (Martel 2012) (*M12*) is shown as an analogue composition of Bezymianny pre-eruptive melt in equilibrium with the phenocrysts

Amphibole's record of the shallow magma storage conditions

All amphiboles in Bezymianny's 1956 eruption products are partly decomposed, which has been interpreted to record reheating to ~ > 1000 °C at a moderately high to high pressure of > 400 MPa (Plechov et al. 2008 for amphibole from blast samples) or final low-pressure storage of magmas (at ≤ 150–200 MPa and probably ~ 75 MPa for amphibole from C-PDC pumices) shortly before eruption (Shcherbakov et al. 2013). We argue against formation of the amphibole decomposition rims by heating to ~ 1000 °C at > 400 MPa, as proposed by Plechov et al. (2008), since this would indicate dramatically different heating events for magmas of the blast and the pumiceous C-PDC, with more significant heating for the blast magma (with thick Type-2 decomposition rims). Blast and pumice samples have the same bulk-rock composition, equivalent phenocryst proportions, and range of amphibole compositions (including core and rim compositions) that calculate equivalent temperatures (Fig. 7; SM2), which suggests that the blast and pumice magmas had closely comparable temperatures. We concur with Shcherbakov et al. (2013) in that the amphibole rims formed at low pressure, yet probably also at increased temperature, as discussed in detail later on.

Like Shcherbakov et al. (2013), we posit that the Type-1 but also Type-2 amphibole decomposition rims record decomposition at pressures below the amphibole stability field of ≤ 150–200 MPa. However, going beyond previous observation and interpretation, we suggest that the two amphibole decomposition rim types record subtle differences in low-pressure evolution. The textural and compositional differences of the decomposition rims could record (1) that Type-1 and Type-2 decomposition rims formed at slightly different pressure conditions; and/or (2) that amphibole with Type-1 decomposition rims spent less time at low pressure (< 2–14 days) than amphibole with the Type-2 decomposition rims (< 4–34 days) as it was proposed by Shcherbakov et al. (2013). We do not further evaluate the low-pressure residence time here (but in Ostorero et al. in press), yet suggest that the glass-poor Type-2 amphibole decomposition rims (≤ 5–10 vol% glass) formed at slightly lower pressure (and thus lower volatile content) than the relatively glass-rich Type-1 decomposition rims (≤ 25 vol% glass), consistent with their characteristic presence in blast and Plinian pumice samples, respectively. The high orthoclase content of the Type-2 plagioclase microlites in the decompression rims is consistent with crystallization at very low pressure, whereas the Type-2 pyroxene and magnetite microlite compositions in the decompression rims agree with crystallization/equilibration at slightly lower temperature and/or more oxidizing conditions than for the Type-1 decomposition rims of the pumice samples. That some of the Type-2 amphibole decomposition rims have outer zones that texturally resemble those of the Type-1 rims and that their plagioclase and pyroxene microlite compositions partly overlap with those of the Type-1 microlites is consistent with intermittent magma storage at low and then very low pressure. That the Type-1 and Type-2 amphibole decomposition rims formed at slightly different pressure agrees with their characteristic occurrence in association with quartz microlites and mostly cristobalite, respectively, as further interpreted below. The intermediate Type-1 to Type-2 amphibole decomposition rims in vesiculated blast samples, which comprise both quartz microlites and cristobalite, track intermittent magma storage at shallow and then very shallow level leading up to eruption.

The shallow reservoir: intermittent storage of magma of the post-blast pumiceous C-PDC

The shallow, intermittent storage of the pumiceous C-PDC magma may be refined through the petrology and mineralogy of the pumices and experimentally determined phase relationships, as follows. That the C-PDC pumices contain quartz crystals but no cristobalite suggests intermittent crystallization at pressures ≥ 25 MPa (Martel et al. 2021b) and subsequent magma storage at pressures < 25 MPa (where cristobalite is stable) for durations shorter than about 4 days (Martel 2012). The volatile contents measured in the melt inclusions (in plagioclase, orthopyroxene, titanomagnetite, and amphibole) from the pumices suggest H_2O solubility pressures between 50 and 100 MPa (Fig. 10), in agreement with this interpretation. Considering maximum glass SiO_2 contents of 79–80 wt% (Fig. 6), quartz is stable at ~ 850 °C at 100 MPa and ~ 925 °C at 50 MPa (Martel et al. 2021b), which constrains the pumiceous C-PDC magma storage to these conditions.

Microlite population densities and compositions may help to further refine the crystallization conditions by comparison to well-constrained phase equilibria. A pre-requisite for

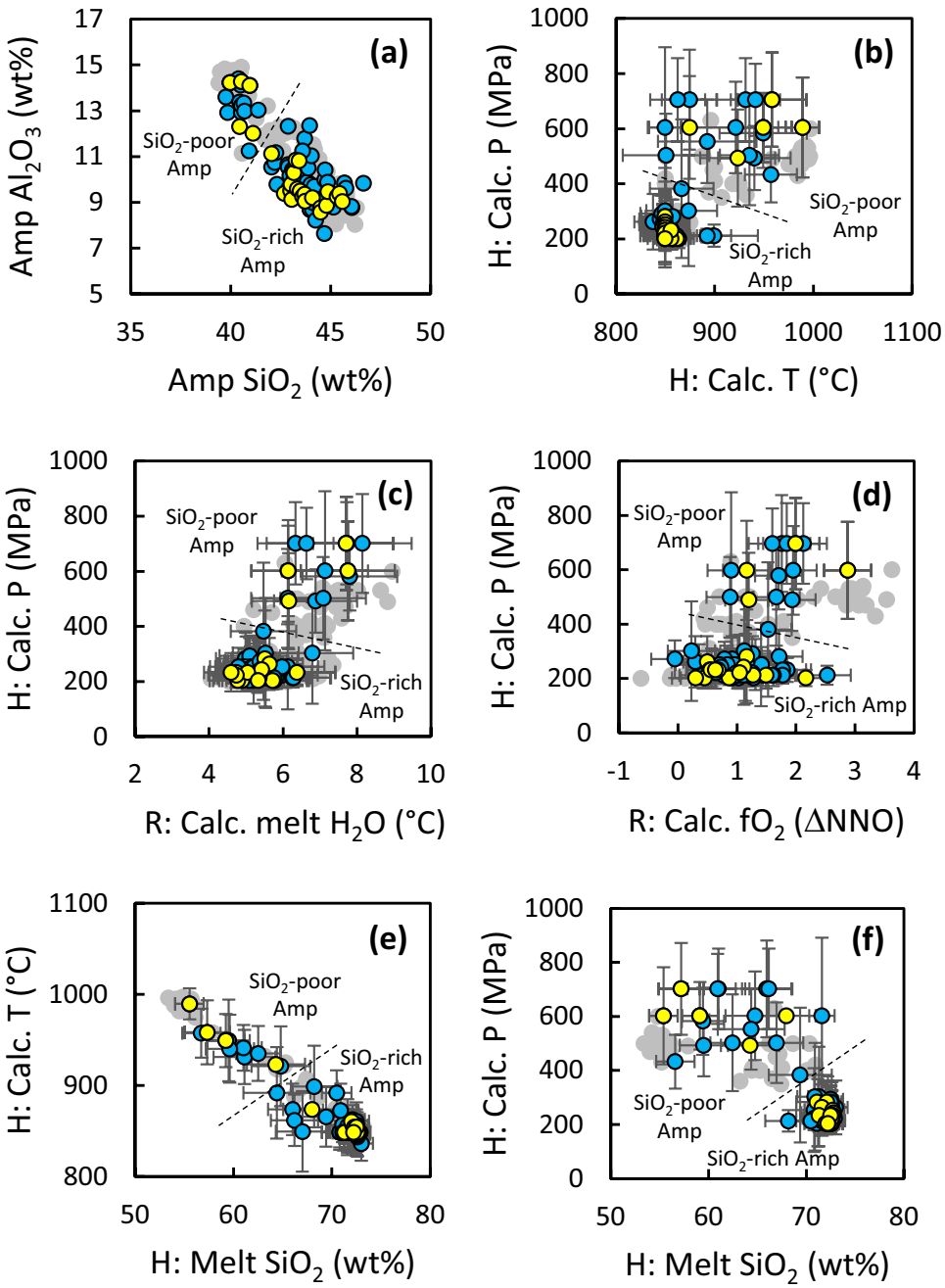

Fig. 7 Amphibole compositions and calculated intensive parameters. **a** Amphibole Al_2O_3 versus SiO_2 amphibole compositions showing significant compositional range with a main Si-rich, Al-poor amphibole population and a minor Si-poor, Al-rich amphibole population. **b** Pressure (P) and temperature (T) calculated using the calibrations of Higgins et al. (2022) (*H*). **c** Pressure versus melt H_2O content. **d** Pressure versus fO_2, **e** temperature versus melt SiO_2, and **f** pressure versus melt SiO_2 content calculated using the calibrations of Higgins et al. (2022) (H) and Ridolfi (2021) (R). Blue and yellow symbols show amphibole compositions from blast and pumice clasts, respectively. The analytical data together with calculated intensive parameters and their estimated uncertainties as well as additional plots are provided in the SM2

this is to determine the composition of the melt from which the microlites crystallized during transfer from the deep to the shallow reservoir, i.e., the composition of the microlite-free residual glass. The composition of the microlite parental melt must be intermediate between that of the melt inclusions (trapped in the deep reservoir during phenocryst growth) and the residual glasses that formed on the way to the surface. From the Harker diagrams (Fig. 6) and the pre-eruptive melt composition experimentally determined at 775 °C and 200 MPa by Shcherbakov et al. (2013), the best estimate for the microlite parental melt composition is close to ~ 76 wt% SiO_2, 13 wt% Al_2O_3, 1.5 wt% CaO, and 6 wt% alkalis. One close analogue to this melt composition is the rhyolitic glass of Mt Pelée volcano that was used by Martel (2012) for constraining low-pressure (25–200 MPa) phase relations (referred as PEL in Fig. 6). The H_2O-saturated PEL phase relations confirm that the plagioclase liquidus composition at a pressure of < 200 MPa is ~ An_{60} (Fig. 11), which matches the more An-rich composition of unzoned microlites or the rims of zoned microlites, in agreement with their faceted tabular shapes evidencing growth at effective undercooling < 50 °C (Hammer and Rutherford 2002;

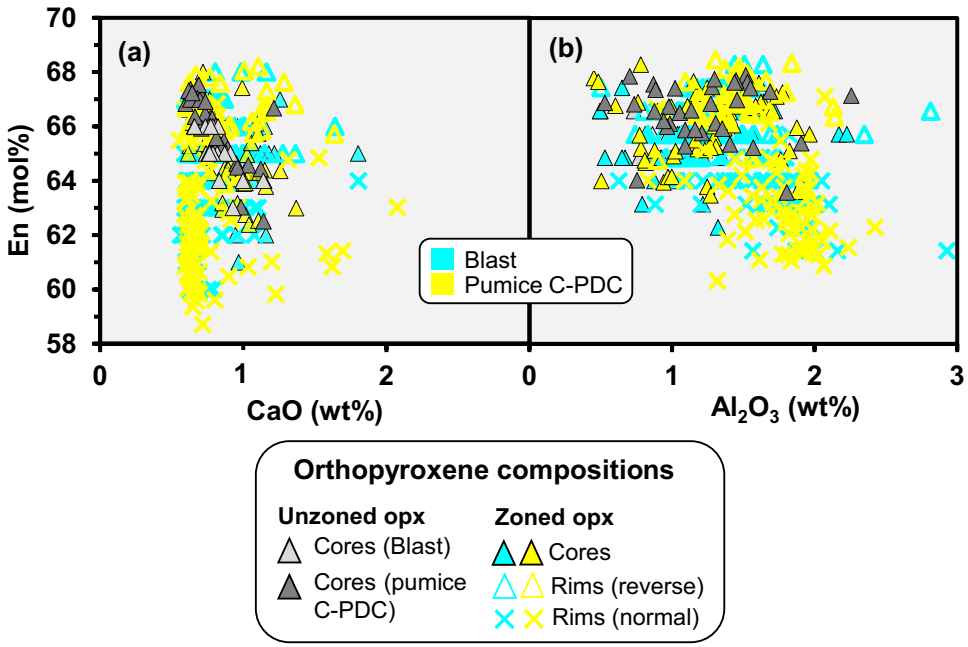

Fig. 8 Orthopyroxene compositions illustrated as the enstatite mol% versus **a** CaO wt% and **b** Al_2O_3 wt%, for unzoned phenocrysts (light grey triangles for blast samples and dark grey triangles for C-PDC pumices) and zoned phenocrysts showing compositions of cores and rims (for reverse and normal zonings); the blue and yellow symbols are for the blast samples and C-PDC pumices, respectively

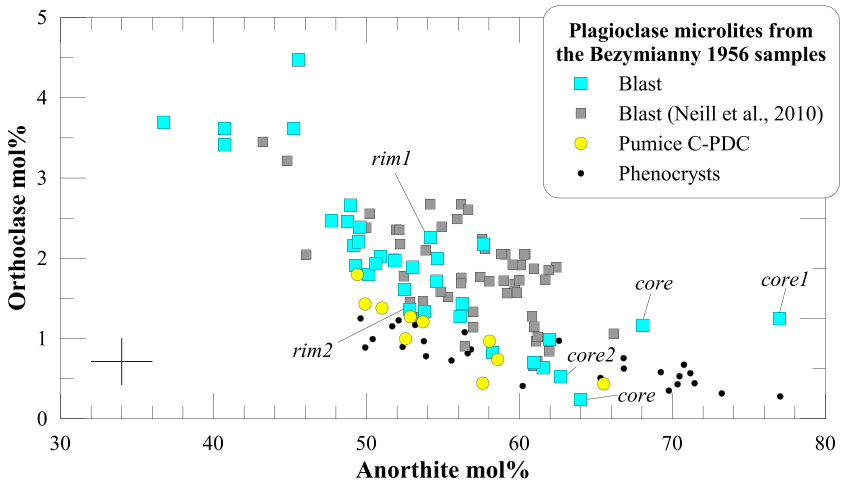

Fig. 9 Plagioclase compositions showing that the microlites in the blast samples extend towards albitic ($An_{36–66}$) and orthoclasic ($Or_{0.5–5.5}$) composition compared to those of the C-PDC pumices ($An_{50–66}$, $< Or_2$), reflecting a higher degree of differentiation. Some microlites from both, blast samples and C-PDC pumices, have cores more calcic ($An_{62–77}$) than the phenocryst rims (~ $An_{50–57;}$ data from the glass-inclusion host plagioclases reported in the SM1), evidencing crystallization from a hotter and/or more mafic melt than the one in equilibrium with the phenocryst rims

Mollard et al. 2012). Yet, plagioclase microlite proportions of ~ 25–35 vol%, as determined in the Bezymianny pumices (Fig. 5), are not replicated experimentally by crystallization of $An_{50–60}$ from the rhyolitic PEL composition, since $An_{50–60}$ follows the plagioclase liquidus with proportions mostly < 5 vol% (Fig. 11). Also, plagioclase compositions richer than ~ An_{65}, as shown by some microlite cores (Fig. 9), cannot crystallize from a rhyolitic liquid of PEL composition (Fig. 11). We therefore suspect, and evaluate further below, that a large proportion of the microlite population crystallized from a more mafic and/or hotter melt likely resulting from a pre-eruptive magma injection in the deep reservoir.

To summarize, we posit that melt inclusion compositions, amphibole decompression rims, the presence of quartz, and absence of cristobalite, may be used to trace magma migration from the upper part of the deep reservoir (~ 200–350 MPa and > 840 °C and likely ~ 860–910 °C) towards intermittent shallower storage at pressures of ~ 50–100 MPa (~ 2–4 km depth). Within the shallow storage zone, the magma temperature was ~ 850–925 °C and the

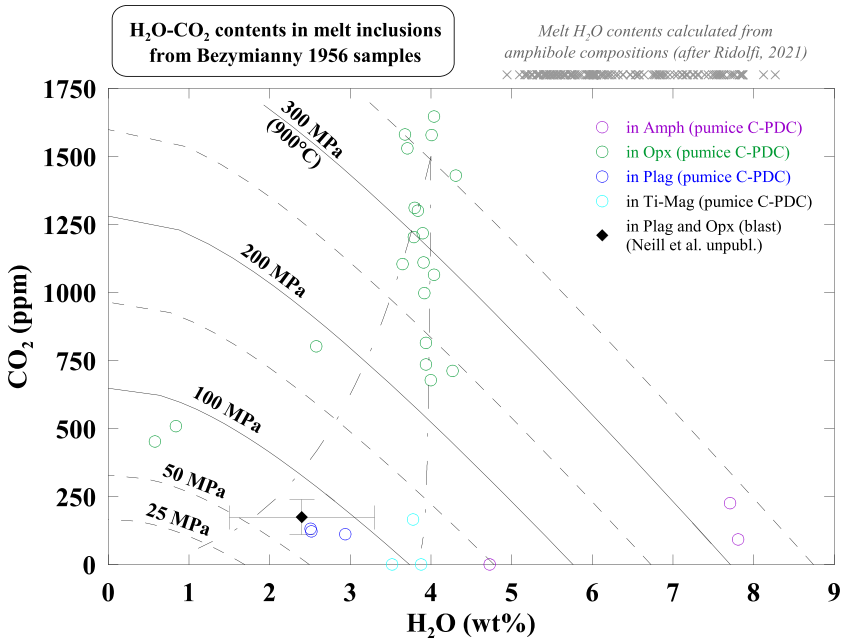

Fig. 10 H_2O and CO_2 contents of phenocryst-hosted melt inclusions. The circles represent data for the 1956 C-PDC pumices. The black diamond shows the mean composition for melt inclusions hosted in plagioclase and orthopyroxene from the 1956 blast samples (Neill et al. unpublished, as mentioned in Shcherbakov et al. 2013) (all data reported in SM1); the given uncertainty on the calculation is about 1 wt% H_2O. Isopleths mark H_2O-CO_2 fluid-saturation pressures and the dash-dot lines simulate degassing paths assuming closed-system degassing (right dash-dot line) and open-system degassing with 10 wt% vapor exsolution (left dash-dot line), calculated at 900 °C in a rhyolitic melt using VolatileCalc (Newman & Lowenstern 2002). The grey crosses above the upper X-axis are H_2O contents calculated from amphibole compositions in Bezy9 pumice samples (this study) and in the blast (Turner et al. 2013) using the formulation of Ridolfi (2021) (i.e., not considering CO_2; data reported in SM2)

melt contained 1.5 to 4.0 wt% H_2O and $CO_2 < 250$ ppm. At these conditions, amphibole partly decomposed to Type-1 rims and the equilibrium melt compared to the most silicic residual glasses of the C-PDC pumices (Fig. 6). The magma that fueled the pumiceous explosive phase of the 1956 eruption is inferred to have rapidly ascended to the surface from storage at this pressure, which we investigate in our companion paper (Ostorero et al., in press).

Magmatic conditions of the cryptodome

The crystallization conditions of the cryptodome may be assessed through the petrology and mineralogy of the 1956 blast fragments and experimentally determined phase relationships, as follows. Like the pumiceous C-PDC magma, the cryptodome magma was stored shortly at 50–100 MPa, as evidenced by minor quartz crystals and locally narrow Type-1 on the main Type-2 amphibole breakdown rims. That the blast clasts contain quartz, as do the C-PDC pumices, suggests that the magma resided for at least some days at pressures of ≥ 25 MPa, as indicated above. The blast clasts, however, predominantly contain large cristobalite, as commonly observed in lava domes (e.g., Boudon et al. 2015), which suggests final crystallization at pressures of ≤ 25 MPa (Martel et al. 2021b). The plagioclase microlites from the blast clasts are richer in Or by about 0.5 to 2.0 mol% with respect to the C-PDC pumices and cover a larger compositional range up to An_{36} (Fig. 9). Among the blast clasts, Neill et al. (2010) also reported that the high-density (less-vesiculated) clasts have microlites with 2–3 mol% higher Or contents at a given An content with respect to the low-density clasts. These An-poor and Or-rich plagioclase microlites in the dense clasts from the blast also correlate with high microlite contents of ~ 40–55 vol% (Fig. 5). Amphibole of the dense blast clasts has moreover thick and pervasive, glass-poor (< 5–10 vol%) breakdown rims (Type-2), which record shallow residence for weeks to months (cf. Plechov et al. 2008) also comprising Or-rich plagioclase microlites. All these observations highlight that the dense clasts underwent more advanced degassing and groundmass crystallization than did the C-PDC pumices or the vesiculated clasts from the blast. At pressures ≤ 25 MPa (≤ 1 km depth), crystallization of ~ 40–55 vol% of ~ $An_{36–60}$ microlites in a ≥ 79 wt% SiO_2 residual melt can be experimentally replicated from the PEL rhyolite at temperatures ≥ 900 °C (Fig. 11). The relevance of such high temperatures is discussed below.

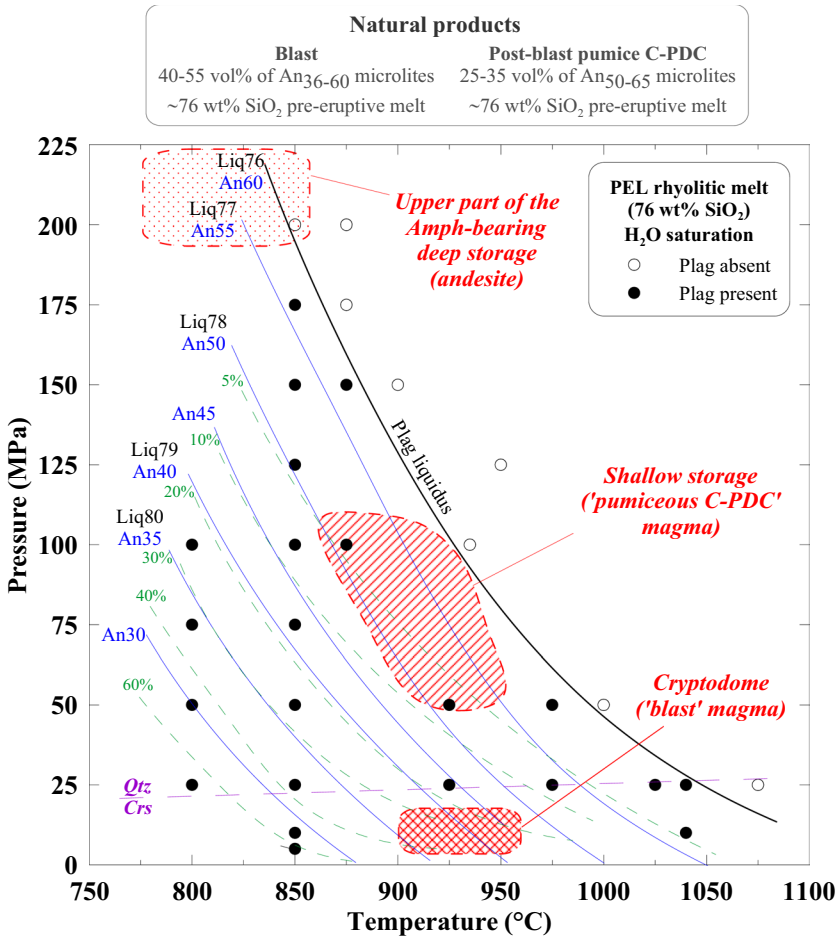

Fig. 11 Rhyolite phase relations using Mt Pelée rhyolitic melt (76 wt% SiO_2) (PEL) showing the SiO_2 content of the residual liquid (black point labels), the plagioclase anorthite content (blue point labels), and the plagioclase volume content (green point labels). Compiled data from Martel (2012) and Martel et al. (2021b). The quartz (Qtz) – cristobalite (Crs) transition is reported following Martel et al. (2021b). The red dashed boxes represent the pressure–temperature conditions proposed for Bezymianny different reservoirs based on the rhyolitic matrix phase-equilibrium data

The 1956 eruption scenario

We conclude that prior to the catastrophic 1956 eruption, Bezymianny's magma was stored in a deep reservoir with the shallow part at ~ 200–350 MPa (i.e., 8–10 km depth). Resident magma stored in the shallow part and recharge magma derived from the lower part of the deep reservoir were at temperatures of ~ 850–990 °C, comprised ~ 35 vol% phenocrysts on average and a residual melt with 76 wt% SiO_2 saturated with ~ 4.0–8.0 wt% H_2O and up to ~ 1500 ppm CO_2 (Fig. 12). Degassing-induced crystallization during upward magma transfer would have resulted in the crystallization of plagioclase microlites more albitic than the phenocrysts and residual melts more differentiated than the melt inclusions (i.e., > 76 wt% SiO_2). In contrast, the plagioclase microlites from the C-PDC pumices and blast clasts have compositions close to the phenocryst rims ($An_{50–60}$), which requires crystallization close to the plagioclase liquidus with resulting crystal contents < 5 vol%. Consequently, the majority of plagioclase microlites do not result from degassing-induced crystallization from the rhyolitic melt. Rather, they may have crystallized from a more mafic and or hotter melt (coming from the deep reservoir) while mixing with the colder resident rhyolitic melt. The C-PDC pumices and blast clasts contain overlapping microlite number densities (~ 10^{12} and $10^{12–13}$ m^{-2}, respectively; Fig. 5b) indicating that the microlites crystallized at similar conditions in the shallow reservoir.

That the blast clasts contain quartz and cristobalite argues in favor of a magma batch migrating from the quartz-stable shallow reservoir to a cristobalite-stable cryptodome at a depth < 1 km below the summit (Fig. 12). Before the blast explosion, the cryptodome magma resided at least some days (duration required for cristobalite formation; Martel 2012), likely weeks (as suggested by the thick Type-2 amphibole decomposition rims; our observations; cf. Plechov et al. 2008), during which the plagioclase microlites further differentiated (An poorer and Or richer than in the C-PDC pumices; Fig. 9) and grew (volume contents from 25 to 50 vol%, as opposed to 20–30 vol% in the C-PDC pumices; Fig. 5). Important deformation of the southeastern slope of the volcanic cone was observed a few months before the eruption (uplift of about 100 m from the photographs in February 1956; Belousov and Belousova 1998; Belousov et al. 2007), probably reflecting the emplacement of a cryptodome in the volcanic flank. The growing cryptodome triggered a flank

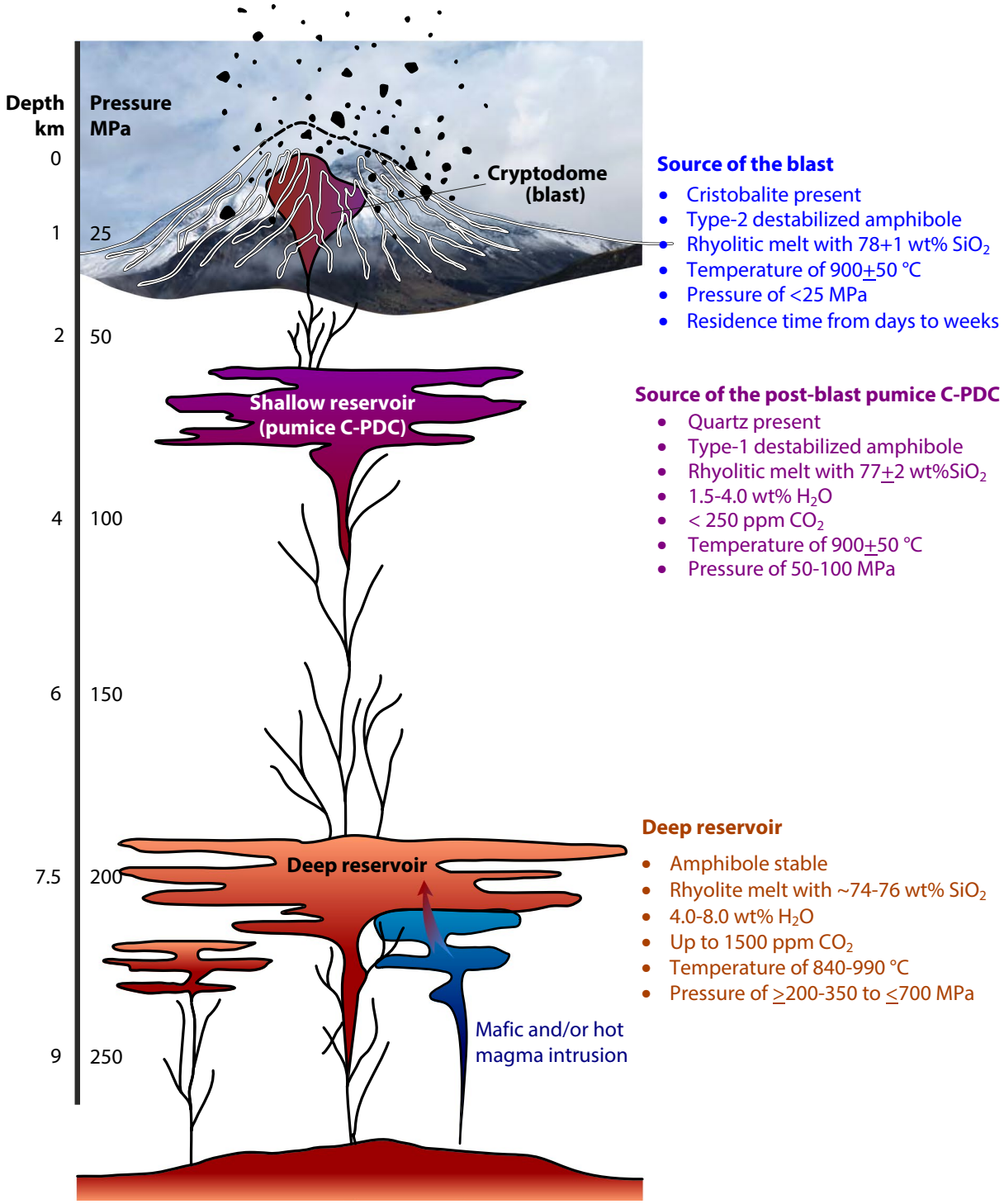

Scheme of Bezymianny plumbing system prior to the 1956 eruption, showing a three-level magma storage architecture comprising a deep andesitic reservoir with a roof located at ~ 7.5 km in depth (~ 200–350 MPa and ~ 840–990 °C, up to 1500 ppm CO_2), a shallow reservoir at 2–4 km deep (50–100 MPa, 900 ± 50 °C, presence of quartz and Type-1 amphibole) in which the cryptodome magma initially resided and from which the post-blast pumiceous magma originates, and a subsurface cryptodome at depth < 1 km (< 25 MPa, 900 ± 50 °C, presence of cristobalite and Type-2 amphibole) from which the laterally directed blast was initiated. Temperature increase between the deep and the shallower reservoirs (up to 900 °C) likely results from the deep injection of a hotter and/or mafic magma

collapse that violently decompressed and fragmented the magma, generating a laterally directed blast on March 30, 1956. The decompression wave reached the shallow reservoir, leading to the eruption and emplacement of post-blast pumice C-PDC, following a scenario illustrated in Fig. 12. The timescales of the proposed pre-eruptive magma dynamics are refined in our companion paper using orthopyroxene and magnetite zoning patterns and amphibole decompression rims (Ostorero et al. in press).

Comparison to Bezymianny's recent eruptions

Based on tomography results using recent (2009–2015) seismic data, Koulakov et al. (2017) suggested the presence of a basaltic reservoir at a depth of 25–30 km below the Klyuchevskoy group of volcanoes, which may be the feeder zone for the basaltic andesites of Bezymianny's recent eruptions (Turner et al. 2013; Davydova et al. 2017, 2022). If this reservoir was also present in the past, it could have been the source of the mafic melt that intruded the reservoirs prior to the 1956 eruption. By examining the earthquake locations below Bezymianny, Thelen et al. (2010) proposed a top of the deep magma chamber at ~ 6 km depth during the eruptive sequence in late 2007, and Koulakov et al. (2021) proposed a deep reservoir at ~ 8 km depth prior to the December 2017 explosive eruption, which both compare to our petrological constraints for the 1956 upper part of the deep reservoir. Koulakov et al. (2021) also proposed the presence of a shallow magma chamber located at 2–3 km depths for the December 2017 eruption, which agree with the inferred 1956 petrological pressure/depth of the shallow reservoir.

Therefore, the magma storage zones inferred from petrological constraints for the 1956 climactic eruption may have been close to those of the plumbing system proposed for the recent eruptions, i.e., a 25–30 km source of basaltic magmas feeding a deep reservoir with a top at 6–8 km depth, intermittently connected to a ~ 2–3 km shallow reservoir and the post-1956 lava dome. Yet, the 1956 eruptions emitted andesites, whereas basaltic andesites are emitted since the 1980s (both magmas contain mafic enclaves; Davydova et al. 2017, 2022) This suggests that the residence timescales of the 1956 magma in the different reservoirs were long enough for differentiation, promoted by either lower magma supply rates or lower magma ascent rates than for the recent eruptions.

Comparison to other blast eruption dynamics

The Bezymianny 1956 laterally directed blast has been compared to the well-documented (video and space imagery) Mt St Helens 1980 and Soufriere Hills 1997 blasts (Belousov et al. 2007), with the conclusion that these laterally directed blasts were all triggered by rapid decompression caused by a large-scale failure of the volcanic edifice. The Bezymianny 1956 magma did not nucleate many microlites in the cryptodome, likely because the decompression from the shallow reservoir to the cryptodome energetically fostered growth around existent crystals at the expense of nucleation (requiring higher effective undercoolings; Martel 2012).

Whether the laterally directed explosion is followed by a pumiceous explosive phase likely depends on the decompression magnitude, the involved magma volumes, and the availability of magma below the lava dome. At Bezymianny in 1956, magma was stored at shallow level (~ 2–4 km depth), which likely favored the explosive event. This event, however, occurred not as a sustained vertical Plinian eruption column, but as a "boiling-over" pumice C-PDC (formed by the immediate gravitational collapse of the overloaded eruption cloud). The observed 35 km-high cloud of the eruption (Gorshkov 1959) represented a giant convective cloud that ascended above a 500 km^2 large area engulfed by the blast D-PDC and the post-blast C-PDC. At Mt St Helens, Plinian activity commenced about an hour or more after the flank collapse and the blast (Lipman and Mullineaux 1981; Criswell 1987), with a magma coming from a reservoir around 7–12 km beneath the summit, as suggested by mineralogical and seismic evidence (Scandone and Malone 1985). At Mt Pelée, the post-blast P1 Plinian magma was directly sampled from the main reservoir (~ 8 km depth), which likely required a stronger decompression wave than required for Bezymianny 1956. Yet, the Mt Pelée 1902 blast was not followed by a pumiceous explosive event, although showing characteristics similar to the P1 blast (volume and extension of the deposits; Boudon and Balcone-Boissard 2021; and sample textures; Martel and Poussineau 2007), highlighting different decompression conditions and/or magma supply.

Conclusions

The pressure (depth) and temperature conditions, as well as the melt volatile and redox conditions of the plumbing system beneath Bezymianny were investigated from a multiphase petrological point of view using amphibole thermobarometry and chemometry, amphibole decomposition rims, matrix glass and melt inclusion compositions, and microlite textures and compositions, using clasts deposited by the blast and the post-blast C-PDC during the climactic phase of Bezymianny 1956 eruption. A three-level magma storage architecture below Bezymianny is inferred with a deep reservoir (≥ 200 MPa and ≥ 840 °C), a shallow reservoir (50–100 MPa and ~ 900 °C) in which the cryptodome magma initially resided and from which the magma of the post-blast pumice C-PDC originates, and a subsurface cryptodome (< 25 MPa and ~ 900 °C) from which the laterally

directed blast was initiated. The three-stage architecture proposed for the 1956 plumbing system compares to the present-day configuration, as imaged geophysically or constrained petrologically for recent mafic eruptions. Therefore, concluding that Bezymianny's plumbing systems prior to the 1956 and prior to the recent eruptions had the same or similar architecture suggests that the timescales of the eruptive dynamics (e.g., magma residence time and ascent rate) may be the key for eruption of evolved or mafic magmas.

Supplementary Information The online version contains supplementary material available at https://doi.org/10.1007/s00445-025-01802-7.

Acknowledgements CM and SE would like to warmly thank I Di Carlo for help with the EMP and Raman analyses and P Benoist and S Janiec for sample preparation and help with the SEM analyses. GB, HBB, LO, and TdA would like to thank S Hidalgo for her help with sample preparation, O Boudouma and S Borensztajn for SEM imaging, E Delairis for the realization of the thin sections, and M Fialin and N Rividi for assistance during EMP analyses. All the authors are grateful to AC Laurent for designing the framework of the final figure. The authors are grateful to the two anonymous reviewers for their fruitful comments that improved the manuscript, and the authors thank the editors, M Edmonds and JE Gardner, for the editorial handling.

Funding Open access funding provided by Université d' Orleans. This project has benefited from financial support from the ANR V-CARE project (ANR-18-CE03-0010; G Boudon) which funded the field mission in Kamchatka, the Institut de Physique du Globe de Paris (IPGP), the EQUIPEX PLANEX project (ANR-11-EQPX-0036; B Scaillet), the LABEX VOLTAIRE project (ANR-10-LABX-100–01; B Scaillet), the expertise and the facilities of the Platform MACLE-CVL co-funded by the European Union and Centre-Val de Loire Region (FEDER), and the French Ministry of Higher Education and Research and Innovation for the doctoral grants of L Ostorero and T d'Augustin.

References

Almeev RR, Ariskin AA, Kimura J-I, Barmina GS (2013a) The role of polybaric crystallization in genesis of andesitic magmas: phase equilibria simulations of the Bezymianny volcanic subseries. J Volcanol Geotherm Res 263:182–192. https://doi.org/10.1016/j.jvolgeores.2013.01.004

Almeev RR, Kimura J-I, Ariskin AA, Ozerov AY (2013b) Decoding crystal fractionation in calc-alkaline magmas from the Bezymianny Volcano (Kamchatka, Russia) using mineral and bulk rock compositions. J Volcanol Geotherm Res 263:141–171. https://doi.org/10.1016/j.jvolgeores.2013.01.003

Balcone-Boissard H, Boudon G, Blundy JD, Martel C, Brooker RA, Deloule E, Solaro C, Matjuschkin V (2018) Deep preeruptive storage of silicic magmas feeding Plinian and dome-forming eruptions of central and northern Dominica (Lesser Antilles) inferred from volatile contents of melt inclusions. Contrib Mineral Petrol 173:101. https://doi.org/10.1007/s00410-018-1528-4

Belousov A (1996) Deposits of the 30 March 1956 directed blast at Bezymianny volcano, Kamchatka, Russia. Bull Volcanol 57:649–662. https://doi.org/10.1007/s004450050118

Belousov AB, Belousova MG (1998) Bezymyannyi eruption on March 30, 1956 (Kamchatka): sequence of events and debris-avalanche deposits. Volcanol Seismol 20:29–47

Belousov A, Voight B, Belousova M (2007) Directed blasts and blast-generated pyroclastic density currents: a comparison of the Bezymianny 1956, Mount St Helens 1980, and Soufrière Hills, Montserrat 1997 eruptions and deposits. Bull Volcanol 69:701–740. https://doi.org/10.1007/s00445-006-0109-y

Boudon G, Balcone-Boissard H (2021) Volcanological evolution of Montagne Pelée (Martinique): a textbook case of alternating Plinian and dome-forming eruptions. Earth-Sci Rev 221:103754. https://doi.org/10.1016/j.earscirev.2021.103754

Boudon G, Komorowski J-C, Villemant B, Semet MP (2008) A new scenario for the last magmatic eruption of La Soufrière of Guadeloupe (Lesser Antilles) in 1530 A.D. Evidence from stratigraphy radiocarbon dating and magmatic evolution of erupted products. J Volcanol Geotherm Res 178:474–490. https://doi.org/10.1016/j.jvolgeores.2008.03.006

Boudon G, Balcone-Boissard H, Villemant B, Morgan DJ (2015) What factors control superficial lava dome explosivity? Sci Rep 5:14551. https://doi.org/10.1038/srep14551

Bouvier A-S, Métrich N, Deloule E (2010) Light elements, volatiles, and stable isotopes in basaltic melt inclusions from Grenada, Lesser Antilles: inferences for magma genesis. Geochem Geophys Geosyst 11:Q09004

Coppola D, Laiolo M, Massimetti F, Hainzl S, Shevchenko AV, Mania R, Shapiro NM, Walter TR (2021) Thermal remote sensing reveals communication between volcanoes of the Klyuchevskoy Volcanic Group. Sci Rep 11:13090. https://doi.org/10.1038/s41598-021-92542-z

Criswell CW (1987) Chronology and pyroclastic stratigraphy of the May 18, 1980, eruption of Mount St Helens, Washington. J Geophys Res 92:10237–10266

d'Augustin T (2021) Les éléments halogènes dans les magmas, du traçage des conditions de stockage aux flux éruptifs. PhD thesis, Sorbonne Université, p 315

Davydova VO, Shcherbakov VD, Plechov PY, Perepelov AB (2017) Petrology of mafic enclaves in the 2006–2012 eruptive products of Bezymianny volcano. Kamchatka Petrol 25(6):592–614. https://doi.org/10.1134/S0869591117060029

Davydova VO, Shcherbakov VD, Plechov PY, Koulakov IY (2022) Petrological evidence of rapid evolution of the magma plumbing system of Bezymianny volcano in Kamchatka before the December 20th, 2017 eruption. J Volcanol Geotherm Res 421. https://doi.org/10.1016/j.jvolgeores.2021.107422

DeMets C (1992) Oblique convergence and deformation along the Kuril and Japan Trenches. J Geophys Res 97:17615. https://doi.org/10.1029/92JB01306

Fedotov SA, Zharinov NA, Gontovaya LI (2010) The magmatic system of the Klyuchevskaya group of volcanoes inferred from data on its eruptions, earthquakes, deformation, and deep structure. J Volcanol Seismol 4:1–33. https://doi.org/10.1134/S074204631001001X

Ghiorso MS, Sack RO (1995) Chemical mass transfer in magmatic processes. IV. A revised and internally consistent thermodynamic model for the interpolation and extrapolation of

liquid-solid equilibria in magmatic systems at elevated temperatures and pressures. Contrib Mineral Petrol 119:197–212
Gorshkov GS (1959) Gigantic eruption of the volcano Bezymianny. Bull Volcanol 20:77–109. https://doi.org/10.1007/BF02596572
Gorshkov GS, Bogoyavlenskaya GE (1965) Bezymianny volcano and peculiarities of its last eruptions in 1955–1963. Nauka, Moscow (in Russian)
Hammer JE, Rutherford MJ (2002) An experimental study of the kinetics of decompression-induced crystallization in silicic melt. J Geophys Res, Solid Earth 107:1–23
Higgins O, Sheldrake T, Caricchi L (2022) Machine learning thermobarometry and chemometry using amphibole and clinopyroxene: a window into the roots of an arc volcano (Mount Liamuiga, Saint Kitts). Contrib Mineral Petrol 177:10
Hoblitt RP, Harmon R (1993) Bimodal density distribution of cryptodome dacite from the 1980 eruption of Mount St Helens, Washington. Bull Volcanol 55:421–438
Kadik AA, Maksimov AP, Ivanov AP (1986) Physico-chemical crystallization conditions and genesis of andesites. Nauka, Moscow (in Russian)
Koulakov I, Abkadyrov I, Al Arifi N, Deev E, Droznina S, Gordeev EI, Jakovlev A, El Khrepy S, Kulakov RI, Kugaenko Y, Novgorodova A, Senyukov S, Shapiro N, Stupina T, West M (2017) Three different types of plumbing system beneath the neighboring active volcanoes of Tolbachik, Bezymianny, and Klyuchevskoy in Kamchatka. J Geophys Res Solid Earth 122:3852–3874. https://doi.org/10.1002/2017JB014082
Koulakov I, Plechov P, Mania R, Walter TR, Smirnov SZ, Abkadyrov I, Jakovlev A, Davydova V, Senyukov S, Bushenkova N, Novgorodova A, Stupina T, Ya Droznina S (2021) Anatomy of the Bezymianny volcano merely before an explosive eruption on 20.12.2017. Sci Rep 11(1):1758. https://doi.org/10.1038/s41598-021-81498-9
Launeau P, Robin P-Y (1996) Fabric analysis using the intercept method. Tectonophysics 267:91–119. https://doi.org/10.1016/s0040-1951(96)00091-1
Lipman PW, Mullineaux DR (eds) (1981) The 1980 eruptions of Mount St. Helens, Washington. US Geol Surv Prof Pap 1250:1–844
Martel C (2012) Eruption dynamics inferred from microlite crystallization experiments: application to Plinian and dome-forming eruptions of Mt. Pelée (Martinique, Lesser Antilles). J Petrol 53:699–725. https://doi.org/10.1093/petrology/egr076
Martel C, Poussineau S (2007) Diversity of eruptive styles inferred from the microlites of Mt Pelée andesite (Martinique, Lesser Antilles). J Volcanol Geotherm Res 166:233–254. https://doi.org/10.1016/j.jvolgeores.2007.08.003
Martel C, Bourdier J-L, Pichavant M, Traineau H (2000) Textures, water content and degassing of silicic andesites from recent plinian and dome-forming eruptions at Mount Pelée volcano (Martinique, Lesser Antilles arc). J Volcanol Geotherm Res 96:191–206
Martel C, Pichavant M, Balcone-Boissard H, Boudon G (2021a) Syn-eruptive conditions of the AD 1530 sub-Plinian eruption of La Soufrière of Guadeloupe (Lesser Antilles). Front Earth Sci 9:686342. https://doi.org/10.3389/feart.2021.686342
Martel C, Pichavant M, Di Carlo I, Champallier R, Wille G, Castro JM, Devineau K, Davydova VO, Kushnir ARL (2021b) Experimental constraints on the crystallization of silica phases in silicic magmas. J Petrol 1–18. https://doi.org/10.1093/petrology/egab004
Mollard E, Martel C, Bourdier J-L (2012) Decompression-induced experimental crystallization in hydrated silica-rich melts: empirical models of plagioclase nucleation and growth kinetics. J Petrol 53:1743–1766
Neill OK, Hammer JE, Izbekov PE, Belousova MG, Belousov AB, Clarke AB, Voight B (2010) Influence of pre-eruptive degassing and crystallization on the juvenile products of laterally directed volcanic explosions. J Volcanol Geotherm Res 198:264–274. https://doi.org/10.1016/j.jvolgeores.2010.09.011
Newman S, Lowenstern JB (2002) VOLATILECALC: a silicate melt-H_2O-CO_2 solution model written in visual basic for Excel. Comput Geosci 28(5):597–604. https://doi.org/10.1016/s0098-3004(01)00081-4
Ostorero L, Boudon G, Balcone-Boissard H, Martel C, Erdmann S, Belousov A, Belousova M, Davydova V, d'Augustin T (in press) The 1956 eruption of Bezymianny volcano (Kamchatka). Part II - Magma dynamics and timescales from crystal records. https://doi.org/10.1007/s00445-024-01792-y
Ostorero L (2022) Spatio-temporal dynamics of the magmatic plumbing systems, towards an « early-warning clock ». Application to Dominica island (Lesser Antilles) and Kamchatka (Russia). PhD thesis, Université Paris Cité, p 476
Plechov PY, Tsai AE, Shcherbakov VD, Dirksen OV (2008) Opacitization conditions of hornblende in Bezymyannyi volcano andesites (March 30, 1956 eruption). Petrol 16:19–35. https://doi.org/10.1134/S0869591108010025
Preece K, Gertisser R, Barclay J, Berlo K, Herd RA, Edinburgh Ion Microprobe Facility (2014) Pre- and syn-eruptive degassing and crystallisation processes of the 2010 and 2006 eruptions of Merapi volcano, Indonesia. Contrib Mineral Petrol 168:1061–1086. https://doi.org/10.1007/s00410-014-1061-z
Putirka KD (2008) Thermometers and barometers for volcanic systems. Rev Mineral Geochem 69(1):61–120
Ridolfi F (2021) Amp-TB2: an updated model for calcic amphibole thermobarometry. Minerals 11(3):324. https://doi.org/10.3390/min11030324
Ridolfi F, Renzulli A (2012) Calcic amphiboles in calc-alkaline and alkaline magmas: thermobarometric and chemometric empirical equations valid up to 1130 °C and 2.2 GPa. Contrib Mineral Petrol 163:877–895
Rose-Koga EF et al (2021) Silicate melt inclusions in the new millennium: A review of recommended practices for preparation, analysis, and data presentation. Chem Geol 570:120145
Sauerzapf U, Lattard D, Burchard M, Engelmann R (2008) The titanomagnetite-ilmenite equilibrium: new experimental data and thermo-oxybarometric application to the crystallization of basic to intermediate rocks. J Petrol 49:1161–1185. https://doi.org/10.1093/petrology/egn021
Scandone R, Malone SD (1985) Magma supply, magma discharge and readjustment of the feeding system of Mount St. Helens during 1980. J Volcanol Geotherm Res 23:239–262
Shcherbakov VD, Neill OK, Izbekov PE, Plechov PY (2013) Phase equilibria constraints on pre-eruptive magma storage conditions for the 1956 eruption of Bezymianny Volcano, Kamchatka, Russia. J Volcanol Geotherm Res 263:132–140
Shishkina TA, Botcharnikov RE, Holtz F, Almeev RR, Portnyagin MV (2010) Solubility of H_2O- and CO_2-bearing fluids in tholeiitic basalts at pressures up to 500 MPa. Chem Geol 277:115–125
Thelen W, West M, Senyukov S (2010) Seismic characterization of the fall 2007 eruptive sequence at Bezymianny Volcano, Russia. J Volcanol Geotherm Res 194:201–213. https://doi.org/10.1016/j.jvolgeores.2010.05.010
Turner SJ, Izbekov P, Langmuir C (2013) The magma plumbing system of Bezymianny volcano: insights from a 54 year time series of trace element whole-rock geochemistry and amphibole compositions. J Volcanol Geotherm Res 263:108–121. https://doi.org/10.1016/j.jvolgeores.2012.12.014
Voight B, Glicken H, Janda RJ, Douglass PM (1981) Catastrophic rockslide avalanche of May 18. In: Lipman PW, Mullineaux DR (eds) The 1980 eruptions of Mount St. Helens. Washington, pp 347–377